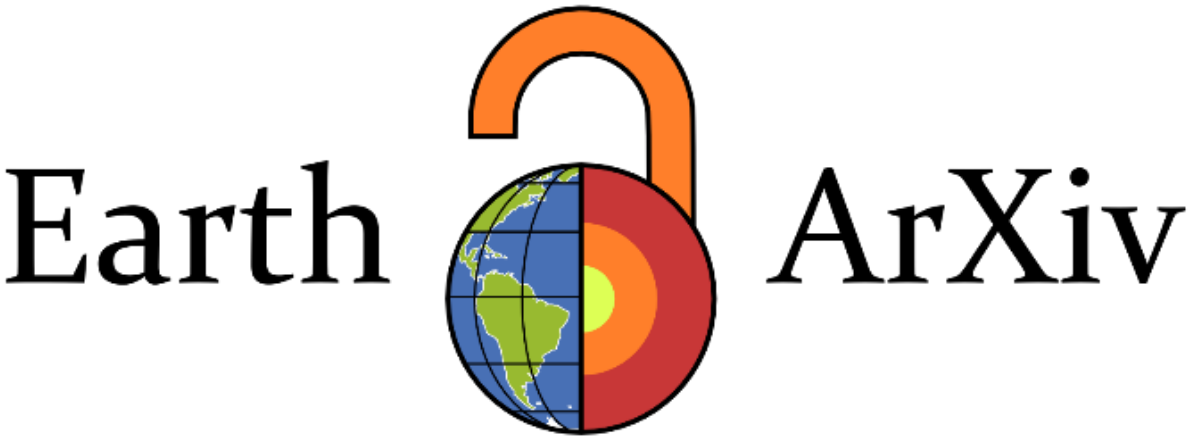


Peer review status:

This is a non-peer-reviewed preprint submitted to EarthArXiv.

Seasonal hydropower forecast framework using a combination of deep learning and physics-based methods

Goutam Konapala[1], Cameron Bracken[1], Nathalie Voisin[1,2]

[1]Pacific Northwest National Laboratory, 902 Battelle Boulevard, Richland, 99352, WA, USA
[2]Department of Civil and Environmental Engineering, University of Washington, Seattle, Washington 98105, USA

Corresponding author: Goutam Konapala (goutam.konapala@pnnl.gov)

Key Points

- We present a prototype converting seasonal forecasts into probabilistic hydropower indicators for regional resource-adequacy planning.
- FNO downscaling lowers monthly spatially averaged errors versus bicubic interpolation, linear scaling, and quantile mapping.
- Hydropower-generation CRPSS is 0.25–0.33 at one month; several snow- and melt-season medians approach or fall below zero by month four.

Plain Language Summary

Seasonal hydropower information can help power-system planners anticipate departures from normal hydropower availability and manage regional resources and costs. We developed a prototype that converts seasonal climate forecasts into probabilistic monthly hydropower

indicators across the contiguous United States by combining machine-learning downscaling, runoff prediction, river routing and water-management modeling, and a statistical generation model. Tests for 2011–2020 showed that the downscaling method reduced average climate-forcing error relative to simpler approaches, although errors remained in complex terrain. Runoff and streamflow checks indicated that uncertainty arises from multiple stages of the modeling chain. Regional hydropower forecasts generally improved on climatology at one month, but skill weakened with lead and varied by region and season. The framework is intended for regional probabilistic resource-adequacy planning rather than plant-level operations because it does not represent plant-specific submonthly operations and constraints.

Abstract

Seasonal hydropower forecasts can inform power-system resource adequacy, but uncertainty propagates through climate, hydrologic, routing, water-management, and generation components. We develop a regional planning prototype linking North American Multi-Model Ensemble seasonal forecasts, Fourier Neural Operator (FNO) downscaling, an uncertainty-aware long short-term memory runoff model based on Uncountable Mixtures of Asymmetric Laplacians (UMAL-LSTM), MOSART-WM routing and water management, and plant-level autoregressive generation estimates. During 2011–2020, FNO reduced monthly spatially averaged mean absolute error relative to the best non-FNO baseline by 13.0% for precipitation, 16.3% for temperature, and 6.2% for wind speed, although residual biases and complex-terrain errors remained. Runoff evaluation showed broad skill relative to the GRFR reanalysis target; independent streamflow and controlled-forcing checks indicated substantial spatial heterogeneity and contributions from both meteorological downscaling and hydrologic-model limitations. Regional hydropower-generation

CRPSS was approximately 0.25–0.33 at a one-month lead. Skill declined with lead and varied by region and season; by month four, several snow- and melt-season regional CRPSS values approached or fell below zero. The framework provides probabilistic hydropower indicators for regional resource-adequacy planning, but it is not a plant-operations model because it does not explicitly represent plant-specific submonthly constraints, flood-control optimization, turbine release versus spill, dynamic hydraulic head, market dispatch, or changing operating priorities.

1. Introduction

Hydropower plays a pivotal role in the U.S. energy portfolio. Hydropower generates approximately 6.5% of the nation's electricity, with significantly higher contributions in certain regions, such as the Pacific Northwest. In energy markets where generators commit to power delivery months in advance, reliable seasonal forecasts of water availability become crucial for hydropower producers [Aasgard et al., 2019; De Silva et al., 2022]. These forecasts inform estimates of potential energy generation over the coming season (e.g., anticipating spring snowmelt runoff or summer low-flow periods) [Hamlet et al., 2002]. This predictive insight directly influences the volume and pricing of long-term contracts that hydropower operators can confidently commit to [Gaudard et al., 2016]. Furthermore, seasonal flow forecasts are essential inputs for resource adequacy assessments performed by grid operators and planners [Sun et al., 2022]. These assessments aim to ensure sufficient generation capacity will be available to meet projected electricity demand over specific future seasons (e.g., assessing resources for anticipated summer peak loads or winter heating demands). However, the inherent uncertainty in predicting water availability for hydropower months in advance, driven by natural climate variability and potential shifts in hydrological regimes influenced by factors such as topography, climate, and land characteristics, complicates this planning process [Schaefli, 2015; Stephens et al., 2021].

Developing accurate and reliable seasonal water availability forecasts that can be applied to forecast hydropower potential presents multi-dimensional challenges. While significant investments have improved shorter-term weather-driven forecasts, accurately predicting streamflow over seasonal timescales remains challenging [Yuan et al., 2015; Troin et al., 2021]. In this direction, the North American Multi-Model Ensemble (NMME) provides a standardized suite of coupled ocean–atmosphere forecasts at monthly time steps, extending out to a 12-month lead time [Kirtman et al., 2014]. While weather prediction skill is poor at these forecast horizons [Mazrooei et al. 2015], skillful hydrologic predictions are feasible several months in advance due to the large-scale climate oscillations (eg, ENSO, PDO) and the integrative nature of hydrologic basins [Wood et al. 2016, Konapala et al., 2020; Bracken et al, 2010, Pechlivanidis et al 2020]. However, the spatial resolution of the constituent models is relatively coarse, typically 1°–2° latitude/longitude, and their native grid cells can span hundreds of square kilometers [Kirtman et al., 2014]. Translating broad climate signals or outputs from numerical weather prediction (NWP) models, which operate at coarser resolutions, into specific, actionable streamflow and hydropower volumes for individual watersheds is complex [Broman et al. 2024, Turner and Voisin 2022]. Additionally, the hydrologic models needed to simulate watershed processes over seasonal timescales are computationally intensive [Cosgrove et al., 2024]. Quantifying this uncertainty in these seasonal hydropower forecasts, which is crucial for risk-based decision-making in both contract negotiation and resource adequacy planning, further increases these computational demands [Lu et al., 2022]. Therefore, continued advancements in seasonal forecasting methodologies, including efficient modeling and robust uncertainty quantification, are critical to support effective long-term hydropower contracting and ensure reliable and economical power grid operations.

Emerging machine learning techniques, particularly deep learning algorithms, offer promising solutions to address the challenges of incorporating localized weather phenomena into coarse-resolution numerical weather prediction (NWP) outputs through downscaling approaches [Rolnick et al. 2019]. Statistical downscaling of climate data using deep learning has attracted much attention over the last few years. As convolutional neural networks [Vandal et al. 2017] and generative adversarial networks [Leinonen et al. 2020] are popular architecture choices for super-resolution images, their variants have become a natural choice for downscaling climate variables. However, Fourier neural operators have recently shown remarkable performance in downscaling meteorological variables with high computational efficiency [Jiang et al., 2023; Yang et al., 2023]. These networks leverage the Fourier transform to capture and represent the frequency components of climate data, enabling efficient and accurate downscaling.

Similarly, Deep Learning algorithms, particularly Long Short-Term Memory (LSTM) algorithms, have successfully modeled the relationship between meteorological variables and runoff [Kratzert et al. 2018]. LSTMs are designed to capture long-term dependencies in sequential data and offer a computationally efficient alternative for operational settings, thanks to their relatively low inference cost [Kratzert et al. 2019]. LSTMs are well-suited for modeling temporal sequences inherent in hydrological processes, such as precipitation-runoff relationships and streamflow patterns. However, accurately representing predictive uncertainty remains a challenge for reliable decision-making. Uncountable Mixtures of Asymmetric Laplacians (UMAL) within the Mixture Density Networks (MDNs) framework provide a model-agnostic approach to quantifying predictive uncertainty for any regression model, including LSTMs [Brando et al. 2022]. Instead of single-value predictions, UMAL estimates the conditional probability distribution of the target variable, given the input. Using Asymmetric Laplacian Distributions (ALDs) allows for modeling

skewed or non-Gaussian error distributions often observed in hydrology, and the "uncountable" mixture removes the need to predefine mixture components. This flexibility enhances UMAL's ability to capture the full range of uncertainty associated with LSTM outputs in hydrological applications [Klotz et al., 2022].

Building on these methods, we develop the workflow in Figure 1 to translate coarse seasonal meteorological forecasts into probabilistic monthly hydropower estimates. The NMME CanESM5 hindcasts are downscaled to 0.1° using FNO trained against MSWX [Beck et al., 2022]. Downscaled meteorology drives a UMAL-LSTM trained against Global Reach-level Flood Reanalysis (GRFR) runoff [Yang et al., 2021], and a seasonal Schaake Shuffle restores spatial and seasonal dependence. MOSART-WM then routes daily runoff and applies large-scale water-management representations to produce monthly inflow, outflow, and storage at hydropower facilities. A plant-level autoregressive model [Bracken et al., 2025] translates those predictors and their annual lags into ensemble generation forecasts at leads of one to four months. The evaluation separates component tests from the end-to-end hydropower assessment so that evidence from a reanalysis target, in-situ observations, and controlled forcing experiments is not conflated.

Section 2 describes the four model components and their data. Section 3 defines the common downscaling baselines, runoff and streamflow tests, controlled forcing experiment, and hydropower metrics. Section 4 reports component and end-to-end results, including seasonal diagnostics. Section 5 states the limitations relevant to operational interpretation, and Section 6 summarizes the conclusions.

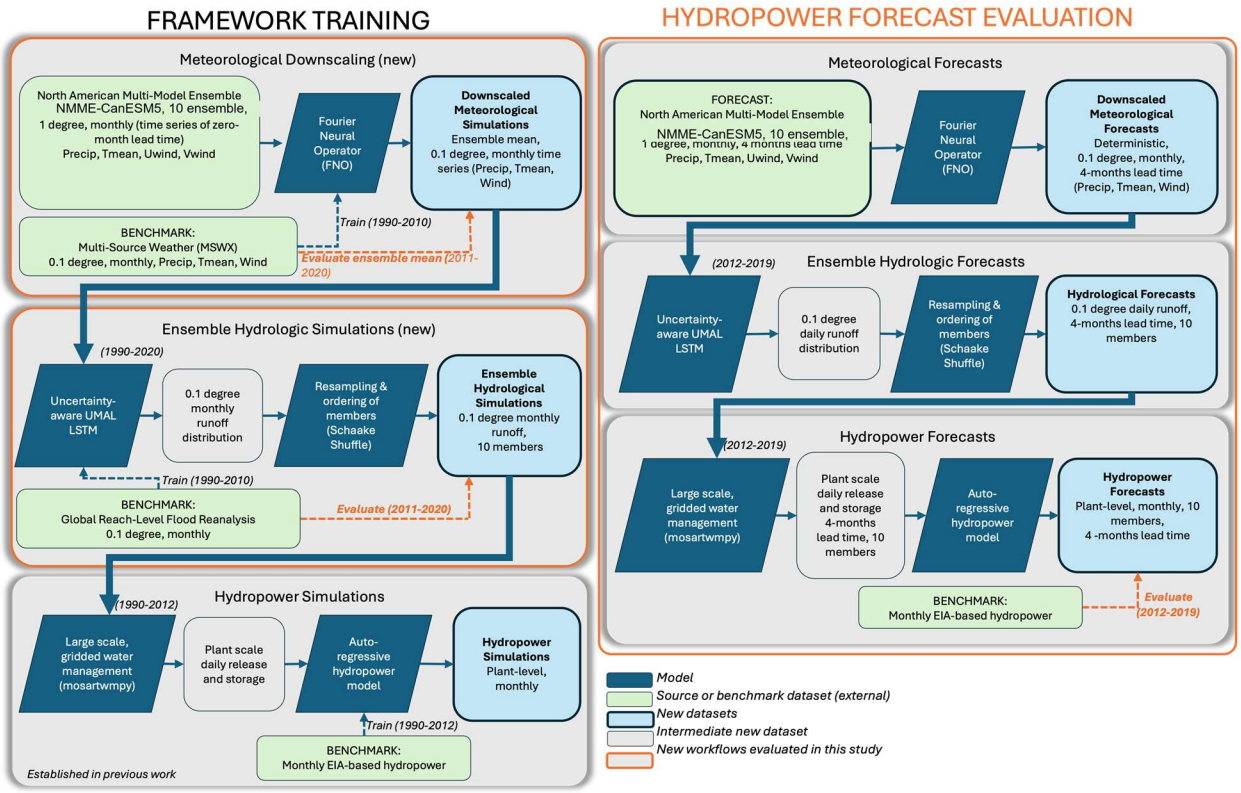


Figure 1: Hydropower Forecasting System Architecture. *Left: training of the meteorological downscaling, hydrological, and hydropower components. Right: application in forecast mode.*

2. Modeling Framework and Data

The workflow comprises four connected components (Figure 1): (1) FNO meteorological downscaling from the NMME CanESM5 hindcasts to 0.1°; (2) probabilistic runoff modeling with UMAL-LSTM and a seasonal Schaake Shuffle; (3) river routing and large-scale water management with MOSART-WM; and (4) plant-level monthly hydropower prediction with an autoregressive model. Each component has a distinct input, calibration target, and evaluation data set, as described below.

2.1 Meteorological Downscaling With a Fourier Neural Operator

For meteorological downscaling, we use precipitation, mean temperature, and the u- and v-components of wind from the Canadian Earth System Model version 5 (CanESM5) hindcasts distributed through the North American Multi-Model Ensemble (NMME) [Kirtman et al., 2014]. MSWX [Beck et al., 2022] provides the 0.1° training and evaluation target. MSWX combines ERA5 reanalysis with monthly 0.1° reference climatologies derived partly from CHELSA (1979–2013). NMME and MSWX monthly data span 1990–2020. Because MSWX is both the calibration and evaluation target, the experiment measures consistency with MSWX rather than independence from biases in its fixed historical reference climatology; operational use under a changing climate would require periodic evaluation against updated station-based observations.

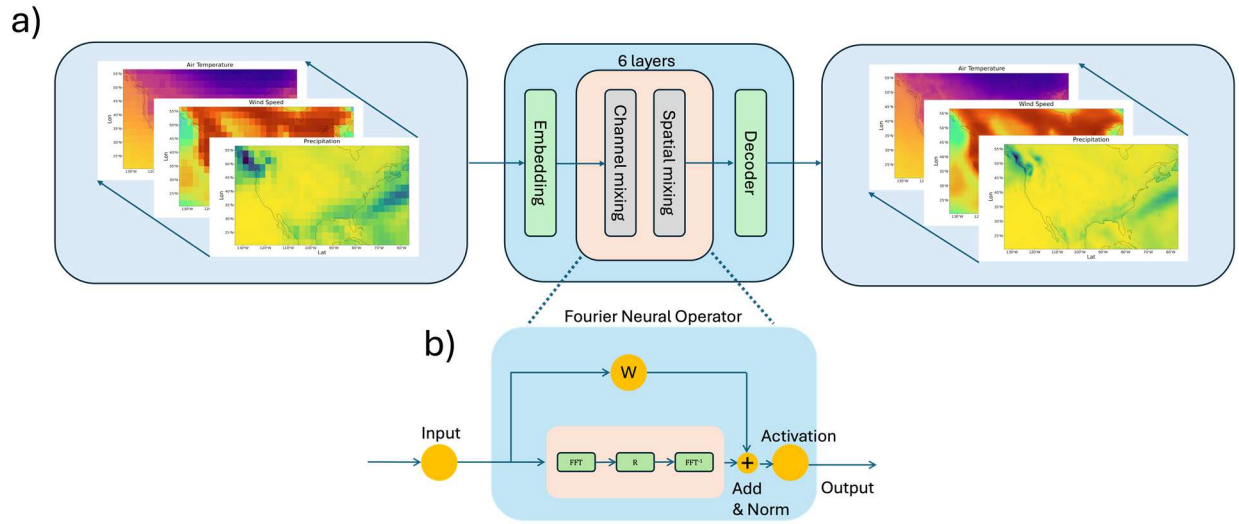


Figure 2: Fourier Neural Operator (FNO) for Meteorological Downscaling. *a) End-to-end downscaling framework showing coarse-resolution inputs (left), FNO architecture with embedding, six-layer network of channel and spatial mixing, and decoder (center), and resulting*

159 *high-resolution outputs (right). b) Core spatial mixing mechanism featuring Fast Fourier*
160 *Transform (FFT), learnable transformation R, inverse FFT, residual connection W, and*
161 *subsequent normalization and activation.*

162 The four monthly NMME variables, precipitation, mean temperature, u-wind, and v-wind, are
163 dynamic inputs. Ten ensemble members are first resampled to the 0.1° MSWX grid, and MERIT
164 DEM elevation [Yamazaki et al., 2019] is included as a static predictor. Inputs and targets are
165 normalized using training-period means and standard deviations. Because MSWX supplies scalar
166 wind speed rather than separate directional components, wind speed is the target for the wind
167 model. Separate FNO models are trained for precipitation, mean temperature, and wind speed. The
168 Fourier layers operate globally in spectral space, allowing each layer to represent long-range
169 atmospheric and topographic dependencies more efficiently than a local convolution with a
170 comparable receptive field [Li et al., 2021].

171 As illustrated in Figure 2a, our downscaling framework processes coarse-resolution
172 meteorological inputs (air temperature, wind speed, and precipitation) through a sophisticated
173 neural architecture. The FNO implementation consists of an embedding layer that processes the
174 input variables, followed by six specialized layers that alternate between channel- and spatial-
175 mixing operations. Channel mixing accounts for interactions among meteorological variables,
176 while spatial mixing captures geographical dependencies. A decoder transforms the processed
177 features into high-resolution (0.1-degree) outputs that accurately represent fine-scale spatial
178 patterns. The core of our approach is the spatial mixing mechanism detailed in Figure 2b. This
179 component implements the Fourier Neural Operator by first applying the Fast Fourier Transform
180 (FFT) to convert spatial data into the frequency domain. A learnable transformation is then applied
181 to these frequencies, enabling the network to selectively modify different frequency components.

The inverse FFT (FFT^{-1}) returns the data to the spatial domain. A residual connection adds the original input to preserve important features, followed by addition, normalization, and activation functions. This mechanism efficiently captures local patterns and long-range dependencies in meteorological fields, yielding physically consistent downscaled outputs that maintain appropriate spatial correlations across the domain.

The embedding layer in our architecture plays a crucial role in harmonizing the different input variables (Prcp, Tmean, UWind, and VWind) and transforming them into a common latent representation with the appropriate dimensionality for subsequent processing. This initial transformation enables the network to effectively leverage complementary information across various meteorological variables. The six-layer structure was determined through extensive experimentation to strike a balance between computational efficiency and model expressiveness. Each channel mixing layer comprises multiple fully connected neural networks that operate independently at each spatial location, enabling complex nonlinear transformations of features across meteorological variables. The spatial mixing layers, implemented using the Fourier mechanism, are particularly advantageous for meteorological downscaling because they can capture local weather patterns influenced by topography and large-scale atmospheric circulation.

The models use grid-based mean squared error during training. Historical data from the 10 NMME ensemble members for 1990–2010 form the training set, and ensemble-mean hindcasts for 2011–2020 form the held-out test set against MSWX. Models are trained for 100 epochs, and the epoch with the lowest validation MAE is retained. The same 2011–2020 months and MSWX target are used for all baseline comparisons described in Section 3.1.

2.2 Probabilistic Runoff Modeling With UMAL-LSTM

We implemented an uncertainty-aware LSTM network that combines the strengths of sequence modeling with probabilistic forecasting to predict daily gridded runoff from monthly meteorological variables. Our approach uses Uncountable Mixtures of Asymmetric Laplacians (UMAL) to quantify predictive uncertainty in LSTM outputs [Brando et al., 2019], yielding comprehensive probabilistic forecasts rather than deterministic predictions. The UMAL-LSTM approach offers several advantages for hydrological forecasting. First, it captures the inherent asymmetry in runoff distributions, where extreme events, such as floods, tend to create right-skewed distributions. Second, it provides complete predictive distributions rather than point estimates, enabling quantification of prediction uncertainty [Klotz et al., 2022].

The input dataset consisted of downscaled monthly time series of meteorological variables (precipitation, temperature, wind) and elevation data at 0.1-degree resolution. The target data is the GRFR gridded daily runoff data resampled to the same 0.1-degree resolution. The LSTM formulation [Brando et al., 2019], as implemented in our framework, is provided in the supplementary material (S1). To extend this architecture for uncertainty quantification, we implement the UMAL approach that models the conditional distribution of runoff given meteorological inputs. Instead of directly outputting a deterministic prediction, the final layer of our network parameterizes a mixture of asymmetric Laplacian distributions:

$$p(y|x) = \sum_{i=1}^{M} \pi_i(x) \cdot AL(y|\mu_i(x), \sigma_i(x), \tau_i(x)) \quad (1)$$

Where M is the number of mixture components, π_i are mixture weights, and each asymmetric Laplacian component AL has location parameter μ_i, scale parameter σ_i, and asymmetry parameter τ_i. These parameters are all functions of the input meteorological variables that the network has

learned. We trained the model using data from 1990 to 2010, utilizing GRFR gridded runoff data at a monthly scale, and validated its performance from 2011 to 2020.

Ensemble runoff forecasts generated by neural networks or processed for probabilistic bias corrections, while capturing forecast uncertainty through multiple realizations, suffer from spatial decorrelation artifacts that degrade the spatial coherence needed for streamflow applications [Clark et al., 2004; Voisin et al., 2011; Schefzik et al., 2013]. The Schaake Shuffle [Clark et al., 2004] addresses this limitation by reordering ensemble forecasts to match the spatial and temporal dependence structures found in historical observations. The Schaake Shuffle differs from empirical copulas in that the multivariable dependence structure comes from observation instead of the raw forecast for copulas. The Schaake Shuffle is a more accurate alternative when quality observed datasets are available [Wilks 2015]. To balance computational efficiency with the preservation of meaningful temporal correlations, we implement a seasonal Schaake Shuffle approach that processes forecasts within climatologically coherent temporal windows. For our implementation, we define four seasons as winter (December, January, February), spring (March, April, May), summer (June, July, August), and Fall (September, October, November). The implementation details and the corresponding performance are provided in the supplemental material (S2) and Supplementary Figure S1.

2.3 River Routing and Water Management

The ensemble gridded runoff estimates are routed daily with mosartwmpy [Thurber et al., 2021], a Python implementation of MOSART-WM. MOSART-WM routes surface and subsurface runoff through hillslopes, tributaries, and main channels in a hierarchical river network [Li et al., 2013; Voisin et al., 2013]. It represents reservoir storage and releases and sectoral water withdrawals and allocation using generic and data-driven large-scale operating rules and updated reservoir data sets

[Voisin et al., 2013, 2017; Turner et al., 2021, 2022]. The configuration includes more than 1,800 reservoirs. Outputs used by the hydropower model, regulated plant-level inflow, outflow, and storage, are aggregated from daily to monthly resolution.

The reservoir operating rules are not dynamically re-optimized using the seasonal forecast. Releases depend on initial storage, prescribed operating priorities, expected seasonal inflow, downstream demand, and observed operating behavior where available [Turner et al., 2021; Broman et al., 2024]. Daily releases and withdrawals are adjusted for maximum-storage and minimum-flow constraints. These representations capture large-scale water management but do not constitute plant-specific, forecast-informed optimization. In particular, the setup does not optimize individual flood-control rule curves or explicitly label each release as turbine flow or spill; unusual events or changed policies may therefore not be reproduced.

2.4 Plant-Level Hydropower Model

The final component is a plant-level monthly autoregressive model trained against historical hydropower generation from the HydroWIRES B1 data set [Bracken et al., 2024; Turner et al., 2022]. It relates generation to MOSART-WM inflow, outflow, storage, and annual lag terms. This is a statistical translation of regulated hydrology into generation, not a plant-dispatch or hydraulic simulation.

$$P_t = \beta_{P,1}P_t + \cdots + \beta_{P,n}P_n + \beta_{O,0}O_t + \beta_{O,1}O_{t-1} \ldots + \beta_{O,n}P_n + \beta_{I,0}I_t + \beta_{I,1}I_{t-1} \ldots + \beta_{I,n}I_n + \beta_{S,0}S_t + \beta_{S,1}S_{t-1} \ldots + \beta_{S,n}S_n + \varepsilon_t \quad (2)$$

In Equation (2), hydropower generation at month t is related to MOSART-WM outflow (O), inflow (I), storage (S), and the specified autoregressive terms. Regression parameters are estimated by ordinary least squares with constraints intended to preserve physical consistency, and a 12-month lag represents recurring annual patterns. Storage is therefore an empirical predictor of generation; the model does not convert storage to reservoir elevation or hydraulic head and does not apply a plant-specific turbine-efficiency curve. At continental scale, translating reservoir storage into water-surface elevation and then time-varying hydraulic head, including forebay and tailwater conditions, remains limited by sparse reservoir-geometry, elevation, and tailwater records [Gao et al., 2012; Hansen et al., 2022]. The model also does not optimize forward release schedules or represent submonthly electricity prices, planned or unplanned outages, infrastructure retrofits, operator forecasts, changing water-use priorities, basin-specific regulation, or non-stationary rule curves. The split sample uses 1990–2012 for parameter estimation and 2013–2019 for validation, reflecting the availability of historical plant-level generation data [Bracken et al., 2025].

3. Evaluation Design

The evaluation follows the modeling chain and addresses three questions: whether FNO improves upon simple spatial and statistical downscaling baselines; whether UMAL-LSTM runoff is skillful against GRFR and how the resulting routed and managed streamflow from mosartwmpy/MOSART-WM compares with in-situ USGS observations when the downscaling step is included or removed; and whether end-to-end hydropower skill remains useful across regions, seasons, and leads of one to four months. Component-specific periods reflect data availability and are stated with each test.

3.1 Meteorological Downscaling Evaluation

FNO is compared with three common benchmarks using the same 2011–2020 test months, ensemble-mean NMME inputs, 0.1° grid, and MSWX target. Bicubic interpolation is a purely spatial resampling benchmark; linear scaling adjusts the mean climatology; and quantile mapping adjusts the modeled empirical distribution toward the reference distribution. For precipitation, temperature, and wind speed, we calculate monthly spatially averaged mean absolute error (MAE) and bias (Equations 3–4) and temporally averaged grid-cell maps. These paired comparisons test error reduction and residual bias separately.

$$MAE = \frac{\sum|y_{FNO} - y_{obs}|}{n} \quad (3)$$

$$Bias = \frac{\sum y_{FNO} - y_{obs}}{n} \quad (4)$$

Where y_{FNO} represents the FNO downscaled values of the ensemble means, y_{obs} represents the MSWX reference values, and n is the number of observations.

To provide a comprehensive assessment, these metrics are analyzed from both a temporal and spatial perspective. We evaluate the temporal evolution of error by computing the spatially averaged MAE and Bias for each month during the validation period (2011–2020). Additionally, we analyze the spatial distribution of error by computing the temporally averaged MAE and Bias for each 0.1° grid cell, allowing for the identification of regional performance patterns.

3.2 Runoff and Streamflow Evaluation

Runoff is first evaluated against the GRFR training target over 2011–2020 to characterize model consistency with the reanalysis product. Deterministic performance uses KGE of the 30-trace ensemble median, and probabilistic performance uses CRPS, CRPSS relative to leave-one-year-

out monthly climatology, and nCRPS. For this GRFR-based runoff analysis, domain-wide and regional median KGE values are calculated from all grid cells. To evaluate the integrated UMAL-LSTM–mosartwmpy chain at the streamflow stage, we separately compare monthly MOSART-WM streamflow with the supplied USGS observations for 2011–2019 at 695 plant–gauge evaluation locations and report the complete USGS KGE distribution. The UMAL-LSTM produces gridded runoff rather than streamflow, and no observations used here isolate its runoff-generation step. Both modeled and observed streamflow can reflect regulation and other management influences; consequently, the USGS KGE represents integrated runoff-generation, routing, and water-management performance rather than a direct evaluation of the UMAL-LSTM. The detailed observational result and its figure are provided in Supporting Information Text S3 and Figures S2–S3.

For the gridded runoff evaluation against GRFR, deterministic UMAL-LSTM performance is computed from the median of 30 traces using the Kling–Gupta efficiency metric. The KGE is defined as:

$$KGE = 1 - \sqrt{(r-1)^2 + (\alpha-1)^2 + (\beta-1)^2} \quad (5)$$

Here r is the Pearson correlation between simulated and observed values, α is the ratio of simulated to observed standard deviation (α = σsim/σobs), and β is the ratio of simulated to observed mean (β = μsim/μobs). KGE = 1 indicates a perfect match. KGE < −0.41 indicates performance below the benchmark obtained by using the observed mean as a constant prediction [Knoben et al., 2019]. For GRFR-based runoff, regional medians and distributions were calculated across the full domain.

Probabilistic performance during the validation period is evaluated using the Continuous Ranked Probability Score (CRPS) [Herbach 2000]. CRPS generalizes the mean absolute error to

probabilistic simulations. For a deterministic simulation, which can be viewed as an ensemble with a single member and zero spread, the CRPS is exactly equivalent to the Mean Absolute Error (MAE). CRPS is computed as

$$CRPS = \frac{1}{m}\sum_{i=0}^{m}|x_i - y| - \frac{1}{2m^2}\sum_{i=0}^{m}\sum_{j=0}^{m}|x_i - x_j| \quad (6)$$

Where m is the number of ensembles from UMAL-LSTM, x_i is the gridded monthly averaged runoff output of ensemble i, and y is the corresponding output from GRFR data. The probabilistic value of the runoff simulation is to be evaluated against an appropriate probabilistic benchmark, namely a climatology ensemble based on the benchmark dataset. The CRPS Skill Score (CRPSS) is computed (Equation 8). We define a climatology benchmark as the monthly value (runoff) over the training and validation period, combined with leaving the validation period simulated year out. The leave-one-year-out is critical for the CRPS, which penalizes heavily when the simulated value is outside of the ensemble spread.

$$CRPSS = 1 - \frac{CRPS_{UMAL-LST}}{CRPS_{Clim}} \quad (7)$$

KGE and CRPSS are computed at each grid cell over the 120 validation months. To diagnose input versus hydrologic-model error, we repeat the evaluation with the same UMAL-LSTM driven directly by 0.1° MSWX meteorology (the No-DS case) and calculate No-DS-minus-FNO differences in both KGE and CRPSS. Positive differences indicate locations where removing the downscaling step improves performance; negative differences show that direct MSWX forcing does not improve the metric. The controlled-experiment details and spatial results are provided in Supporting Information Text S4 and Figures S4–S5.

Additionally, to provide an operator-relevant metric, we provide the normalized Continuous Ranked Probability Score (nCRPS), which is calculated by dividing the CRPS by the magnitude

of the observed runoff at each grid and time point. This normalization approach enables fair comparison of simulation skill across grids by providing a relative measure of the error. The nCRPS is calculated as:

$$nCRPS = \frac{CRPS*100}{R_{obs}} \quad (8)$$

Where CRPS is the Continuous Ranked Probability Score calculated from the validation period, and R_{obs} is the corresponding runoff value.

3.3 Hydropower Evaluation

Plant-level hydropower forecasts are evaluated against observation-based HydroWIRES B1 monthly generation [Bracken et al., 2024; Turner et al., 2022] using CRPSS and nCRPS for leads of one to four months. Facility results are aggregated by North American Electric Reliability Corporation (NERC) region. In addition to full-year summaries, the supplied seasonal diagnostic groups months as NDJFM (snow season), AMJJ (melt season), and ASO (late-summer/early-fall low-flow season). The ASO panel contains three lead months because of the seasonal window. These diagnostics are used to limit conclusions about long-lead value to the regions and seasons where skill remains above climatology. Facility-level seasonal spatial maps are provided in Supporting Information Text S5 and Figures S6–S11.

4. Results

4.1 Deterministic Meteorological Downscaling

4.1.1 Precipitation

Across the 2011–2020 test months, FNO has the lowest aggregate precipitation MAE (0.83) compared with quantile mapping (0.95), linear scaling (1.08), and bicubic interpolation (1.25) (Table 1; Figure 3a). This is a 13.0% reduction relative to the best non-FNO baseline, calculated from unrounded values. FNO also has the smallest signed mean bias (+0.22) and mean absolute monthly bias (0.24) among the four methods. The monthly bias curves still overlap and change sign (Figure 3b), so the result should not be interpreted as uniformly unbiased downscaling.

The spatial distribution of precipitation errors (Figure 4a-b) reveals distinct regional patterns tied to topographic and climatic complexity. The highest MAE values (exceeding 6 mm/day, shown in dark red) are concentrated in the western mountainous regions, including the Cascade Range, Sierra Nevada, and Rocky Mountains. This pattern reflects the well-documented challenge of representing orographic precipitation processes in numerical models [Maraun et al., 2010]. The southeastern United States also exhibits elevated errors, likely associated with convective precipitation processes that are difficult to capture at monthly timescales. The spatial bias pattern shows systematic regional tendencies: negative bias (blue regions) dominates the Pacific Northwest, indicating consistent underestimation of precipitation in this wet region. In contrast, positive bias (red regions) appears in parts of the southwestern and southeastern United States. These patterns suggest that the FNO successfully learns regional climate characteristics but struggles with extreme precipitation gradients.

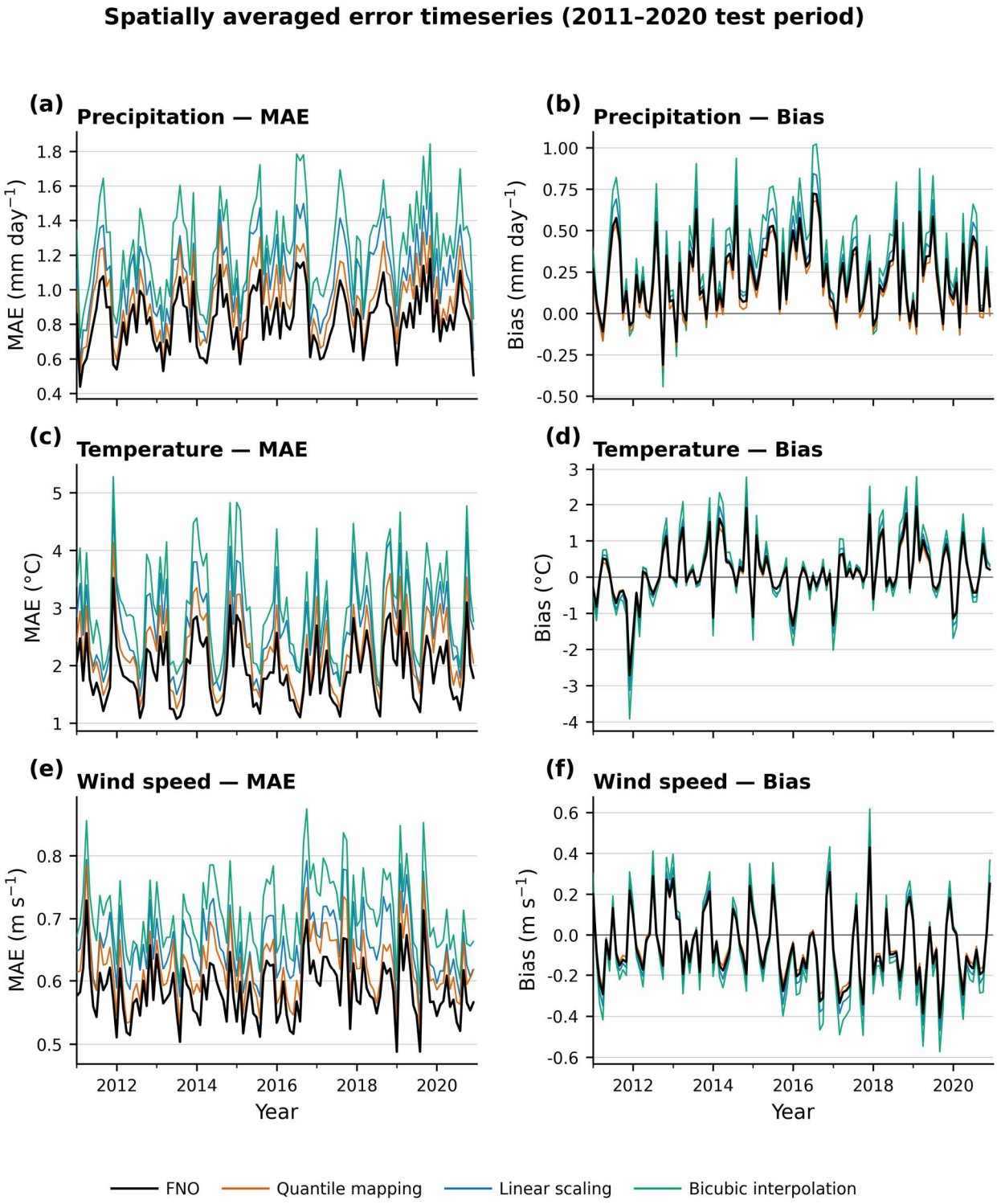
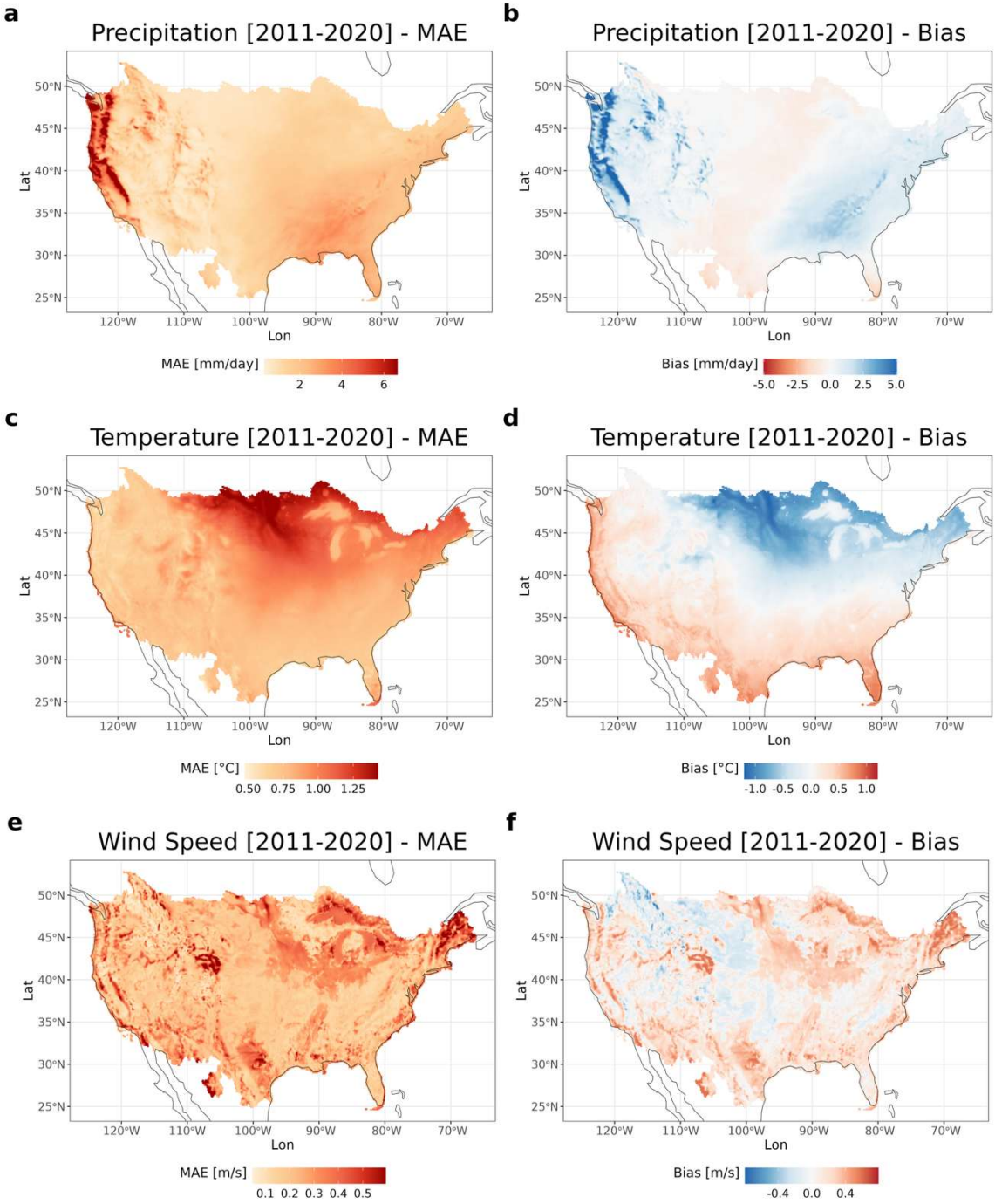


Figure 3. Common-period comparison of meteorological downscaling methods, 2011–2020. *Monthly spatially averaged MAE (left) and bias (right) against MSWX for precipitation (a–b),*

399 *temperature (c–d), and wind speed (e–f). FNO is compared with quantile mapping, linear scaling,*
400 *and bicubic interpolation on the same test months and grid. Lower MAE is better; bias near zero*
401 *is better.*



402

Figure 4: Spatial Distribution of Meteorological Downscaling Errors (2011–2020). Maps showing the temporally averaged spatial distribution of downscaling performance metrics across the continental United States for the validation period. Left panels (a, c, e) display Mean Absolute Error (MAE), and right panels (b, d, f) show bias for precipitation, temperature, and wind speed downscaling, respectively.

4.1.2 Temperature

For temperature, FNO has the lowest aggregate MAE (1.89), compared with 2.26 for quantile mapping, 2.65 for linear scaling, and 3.02 for bicubic interpolation (Table 1; Figure 3c), a 16.3% reduction relative to the best non-FNO baseline, calculated from unrounded values. The bias result is more nuanced: quantile mapping has a slightly smaller signed mean bias (+0.10 versus +0.11 for FNO) and mean absolute monthly bias (0.50 versus 0.54). Thus, FNO's temperature advantage is in MAE and does not extend to every bias metric; the shared seasonal warm and cold excursions in Figure 3d remain.

Spatially, temperature MAE (Figure 4c) shows the highest errors in northern regions and complex terrain areas, with values exceeding 1 °C in parts of the northern Great Plains and mountainous regions. Including elevation as a static input variable effectively captures topographic-temperature effects, as evidenced by generally lower errors across most terrain-following patterns. The temperature bias map (Figure 4d) reveals a distinct north-south gradient, with cold bias (blue) in the north and warm bias (red) in the south. This pattern suggests that the model may not fully capture continental-scale temperature gradients, possibly related to inadequate representation of seasonal snow cover effects or land-atmosphere interactions in the source climate model.

4.1.3 Wind Speed

For wind speed, FNO has the lowest aggregate MAE (0.59), compared with 0.63 for quantile mapping, 0.66 for linear scaling, and 0.71 for bicubic interpolation (Table 1; Figure 3e), a 6.2% reduction relative to the best non-FNO baseline, calculated from unrounded values. FNO also has the signed mean bias closest to zero (−0.06) and the smallest mean absolute monthly bias (0.15). All four methods nevertheless share negative-bias periods and similar temporal excursions (Figure 3f).

The spatial distribution of wind speed MAE (Figure 4e) shows a clear pattern of elevated errors in topographically complex regions, particularly the Rocky Mountains, Appalachians, and parts of the western United States, where values reach up to 0.5 m/s. Coastal regions, especially along the Great Lakes and Atlantic coast, also exhibit higher errors, likely reflecting the challenges in capturing land-sea interaction effects on local wind patterns. The central Great Plains region shows the lowest MAE values, consistent with its smoother topography and more predictable synoptic-scale wind patterns. The spatial pattern of wind speed bias (Figure 4f) reveals a more complex regional structure than the temporal analysis suggests. While the overall bias magnitudes remain small (±0.4 m/s), distinct regional patterns emerge. Negative bias (underestimation) occurs in parts of the northern Great Plains and some mountainous areas, while positive bias (overestimation) predominates in coastal regions and parts of the southwestern United States. These patterns likely reflect the model's varying ability to capture local wind enhancement or sheltering effects caused by topographic features and land-water contrasts.

4.1.4 Overall Downscaling Assessment

The common-period comparison supports FNO as the lowest-MAE method among the selected baselines for all three meteorological variables (Table 1), with reductions of 13.0%, 16.3%, and 6.2% relative to the best non-FNO precipitation, temperature, and wind-speed baselines, respectively; percentages were calculated from unrounded values. It does not show universal superiority in bias, as quantile mapping has slightly lower aggregate temperature-bias metrics. Those QM and FNO temperature-bias values are descriptively close. FNO's lower MAE indicates better overall pointwise agreement over the common test months, but sampling uncertainty was not quantified, so the small bias differences should not be treated as statistically distinguishable or as evidence of better tail behavior. The spatial maps in Figure 4 identify the greatest precipitation and wind errors in complex terrain and regional temperature-bias patterns. Because MSWX is the training and evaluation target, these results quantify agreement with MSWX rather than independent truth and cannot exclude bias inherited from its historical climatology. The downstream controlled-forcing experiment in Section 4.2.2 tests whether bypassing FNO is sufficient to remove runoff errors.

Table 1. Aggregate meteorological downscaling metrics against MSWX for the common 2011–2020 test period. Lower MAE and mean |bias| are better; signed bias closest to zero is better. Units are mm d^{-1} for precipitation, °C for temperature, and m s^{-1} for wind speed. Values are rounded to two decimals; percentage reductions in the text were calculated from unrounded values.

Variable	Method	MAE	Bias	Mean |bias|
Precipitation	**FNO**	**0.83**	**+0.22**	**0.24**
	Quantile mapping	0.95	+0.24	0.27
	Linear scaling	1.08	+0.26	0.29

Variable	Method	MAE	Bias	Mean |bias|
	Bicubic	1.25	+0.32	0.36
Temperature	**FNO**	**1.89**	**+0.11**	**0.54**
	Quantile mapping	2.26	+0.10	0.50
	Linear scaling	2.65	+0.14	0.68
	Bicubic	3.02	+0.16	0.84
Wind speed	**FNO**	**0.59**	**−0.06**	**0.15**
	Quantile mapping	0.63	−0.07	0.16
	Linear scaling	0.66	−0.07	0.18
	Bicubic	0.71	−0.08	0.22

4.2 Runoff and Streamflow

4.2.1 GRFR-Based Deterministic Evaluation

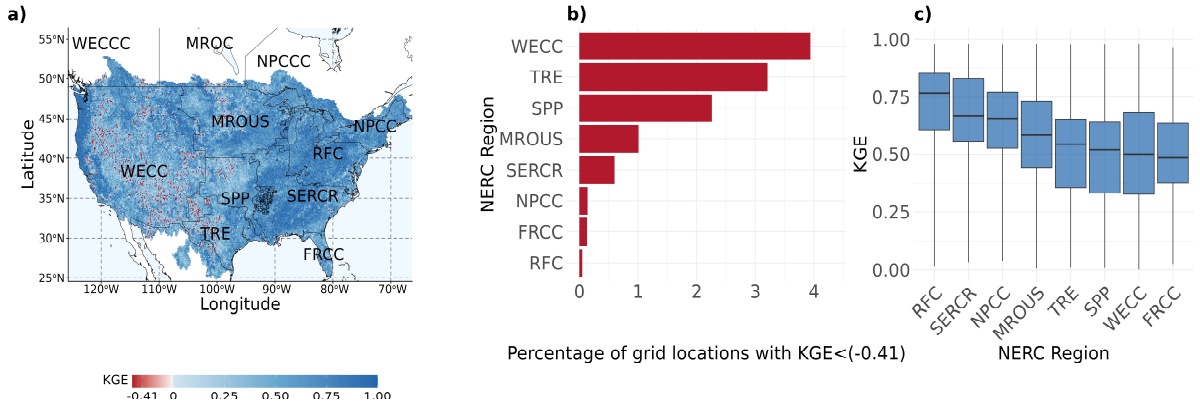
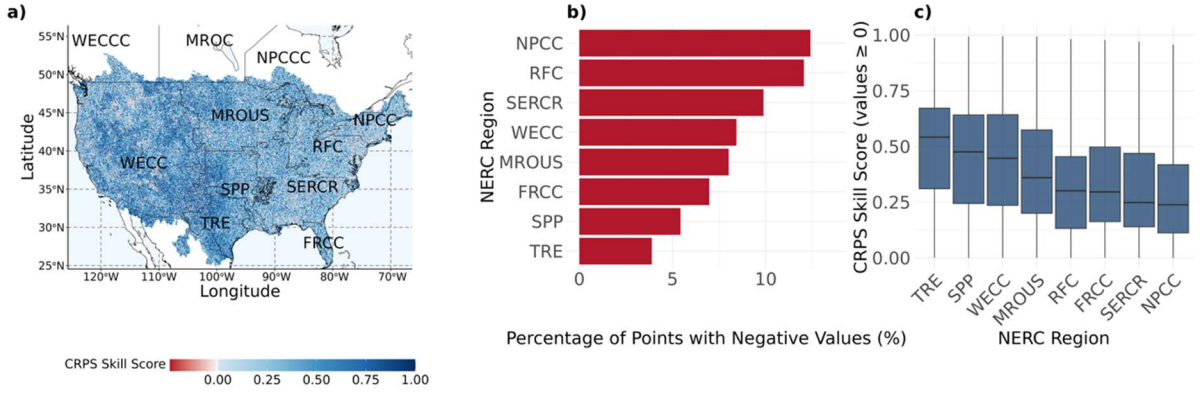


Figure 5. GRFR-based KGE evaluation of the UMAL-LSTM ensemble median across NERC regions. *(a) Spatial KGE over the conterminous United States. (b) Fraction of all grid cells with KGE < −0.41 by region. (c) Regional KGE boxplot distributions by NERC region.*

The GRFR-based map shows broad positive KGE with lower skill in mountain, high-latitude, and transitional regions (Figure 5a). Recalculating the regional medians across the full domain lowered

472 them by about 0.02, from approximately 0.50–0.70 to 0.48–0.68. Figure 5b reports the fraction
473 below the −0.41 observed-mean benchmark, and Figure 5c summarizes the regional distributions.

474 4.2.2 GRFR-Based Probabilistic Evaluation



475

476 ***Figure 6. Spatial and statistical evaluation of CRPSS for the UMAL-LSTM across NERC***
477 ***regions.*** *(a) Spatial CRPSS over the conterminous United States. (b) Fraction of grid cells with*
478 *negative CRPSS by region. (c) Conditional distributions of positive CRPSS by region.*

479 CRPSS ranges from negative values to 1; values below zero indicate no improvement over the
480 climatological reference, and 1 denotes perfect probabilistic skill. The GRFR-based CRPSS map
481 is predominantly positive, indicating that the UMAL-LSTM ensemble generally improves upon
482 the leave-one-year-out climatological reference used in this analysis (Figure 6). Negative skill
483 remains geographically organized and varies by region, reinforcing the need to report the complete
484 distribution rather than only positive values. WECC is especially heterogeneous, consistent with
485 its range of snow regimes and complex terrain.

486 Positive CRPSS values demonstrate probabilistic value relative to the specified GRFR
487 climatology, but this evidence is target-dependent. The nCRPS results in Figure 7 provide a
488 complementary measure of relative error, and the actual-forcing comparison in Section 4.2.2 tests

whether meteorological downscaling is the dominant source of spatial variation. The nCRPS field is hydroclimatically organized and complements the CRPSS pattern: lower nCRPS indicates smaller error relative to runoff magnitude. Eastern and central areas are generally more spatially uniform, whereas the mountainous West spans a wider range of error. This heterogeneity motivates the actual-forcing experiment and cautions against attributing downstream hydropower-season differences to a single upstream source.

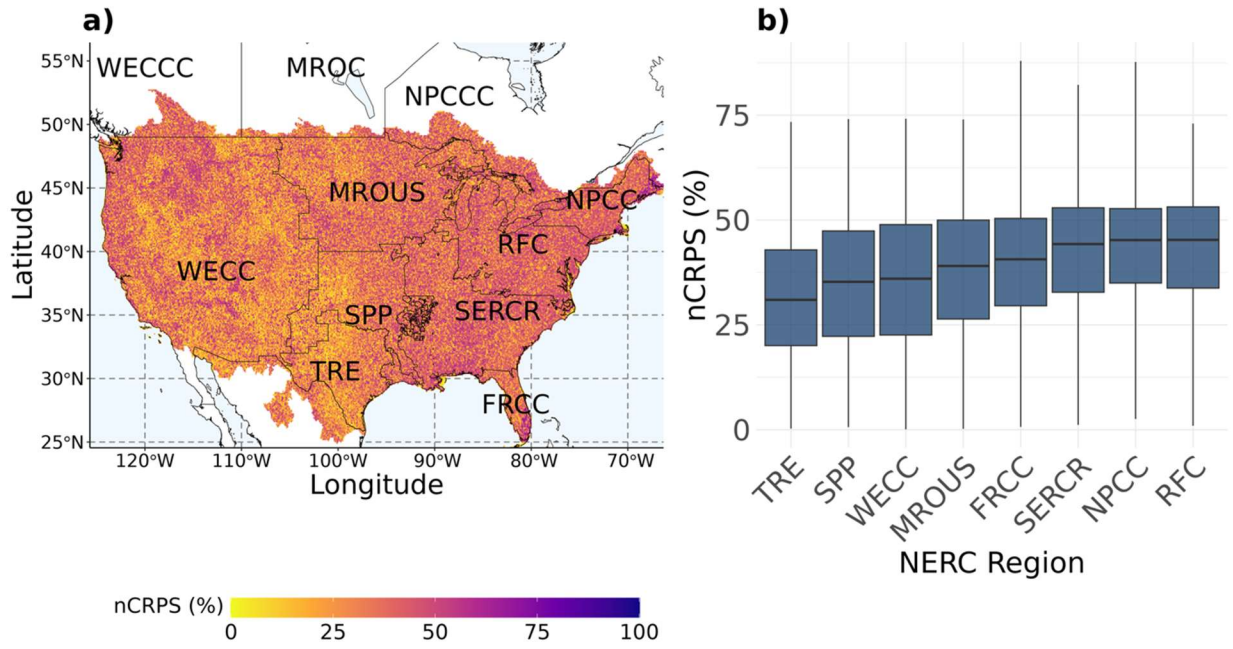


Figure 7. Spatial map and regional distributions of normalized CRPS (nCRPS) for the UMAL-LSTM. *(a) Spatial nCRPS over the conterminous United States (lower is better). (b) Regional nCRPS distributions by NERC region.*

Independent comparison with USGS gauges showed pronounced spatial heterogeneity and an all-location median monthly KGE of 0.38 across 695 supplied plant–gauge evaluation locations (Supporting Information Text S3 and Figures S2–S3). Because the UMAL-LSTM produces runoff

that is subsequently routed and regulated, this observational result evaluates the integrated runoff, routing, and water-management chain rather than UMAL-LSTM runoff alone. Both modeled and observed streamflow can reflect managed conditions. The controlled actual-forcing experiment shows predominantly positive No-DS-minus-FNO differences in both KGE and CRPSS across the domain, including much of the West (Supporting Information Text S4 and Figures S4–S5). Because the same UMAL-LSTM improves when the FNO/downscaling stage is bypassed, the result directly implicates error introduced by that stage as a substantial contributor to the FNO-forced runoff error. Localized non-positive differences show that hydrologic-model, reference-data, and spatial-scale limitations remain.

4.3 Probabilistic Hydropower Forecasts

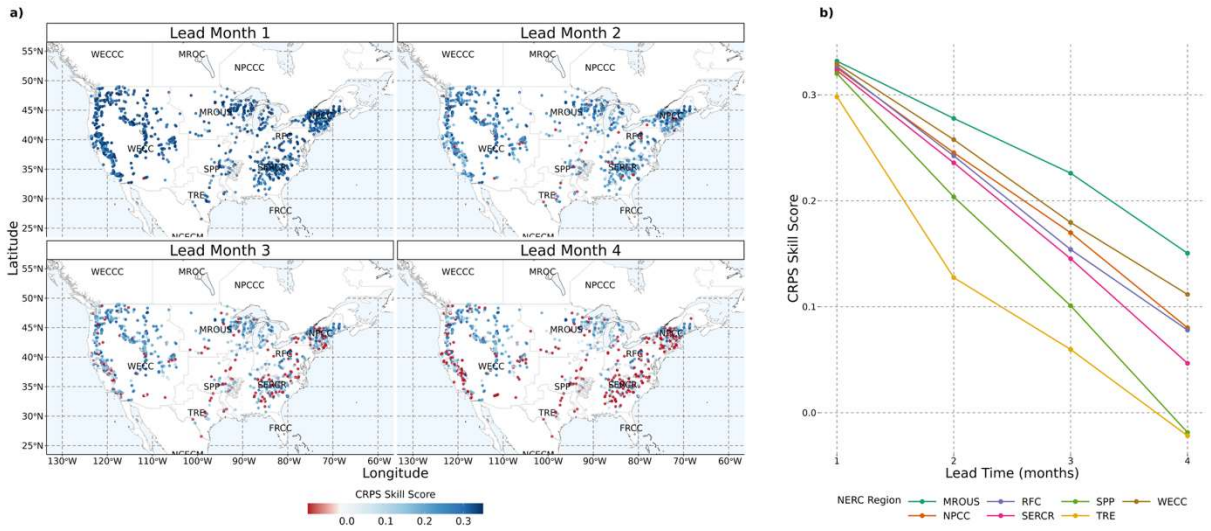


Figure 8. Hydropower-generation forecast skill measured by CRPSS at lead months 1–4. *(a) Facility-level CRPSS at each lead and (b) regional median CRPSS by NERC region. Positive values indicate improvement over the climatological reference.*

Hydropower CRPSS is broadly positive at one month and declines with lead time (Figure 8). By month four, regional median skill is small in several regions and spatially heterogeneous within regions. WECC retains non-zero median skill in the full-year summary, but many western facilities lose skill as meteorological, snow, routing, and operational uncertainties accumulate. These results support one-month regional planning use more strongly than a general claim of useful skill through four months. Complementing the relative-skill view in Figure 8, Figure 9 reports normalized CRPS. At one month, most facilities have nCRPS below approximately 5% of long-term mean monthly generation. Relative error rises with lead and becomes largest in portions of WECC, SPP, and SERCR. By month four, regional medians span approximately 10–25%, with larger values at

some facilities. The widening within-region spreads reinforce the need for facility- and season-aware interpretation.

CRPSS and nCRPS provide complementary information: a forecast can retain positive skill relative to climatology while still having a wide absolute uncertainty band. At one month, both metrics generally support regional planning value. At longer leads, the rising nCRPS and declining CRPSS call for wider uncertainty margins and region-specific interpretation rather than a single nationwide operational threshold. A universal 'good enough' CRPSS threshold is not assigned here; establishing decision-relevant thresholds requires stakeholder engagement and decision-specific loss and cost criteria beyond the scope of this study. The contrast is especially important in WECC, where hydrologic and operational diversity produces large within-region spreads. Storage can buffer hydrologic variability, but at seasonal horizons it also increases operator discretion that the autoregressive model represents only through historical statistical relationships. Consequently, non-zero regional CRPSS at month four does not establish plant-level decision value at every facility.

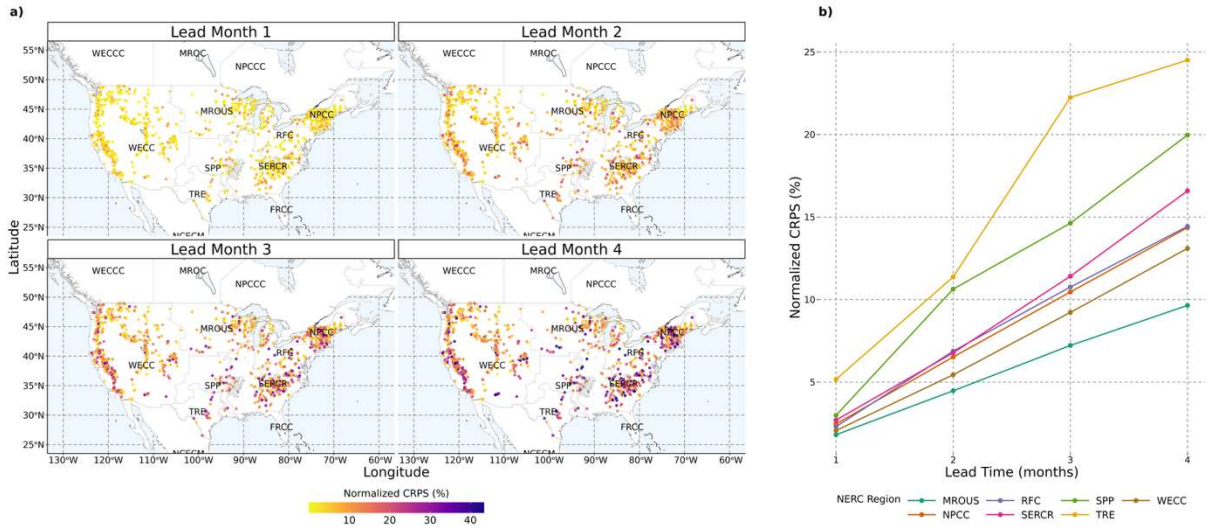


Figure 9. Hydropower-generation forecast error measured by nCRPS. *(a) Facility-level nCRPS (%) at lead months 1–4, where larger values indicate worse relative error. (b) Median nCRPS (%) by lead and NERC region.*

4.3.1 Seasonal and Lead-Time Dependence

Seasonal hydropower-generation diagnostics sharpen the full-year interpretation (Figure 10). At lead month 1, regional median nCRPS is approximately 2–5% and CRPSS is approximately 0.25–0.33 across the plotted seasons. By lead month 4, full-year nCRPS spans about 10–25% and CRPSS ranges from approximately −0.03 to 0.14 across regions. Degradation is stronger during the NDJFM snow and AMJJ melt seasons: SPP, TRE, and WECC reach roughly 30–38% nCRPS at month 4, and several regional CRPSS values approach or fall below zero, while NPCC, RFC, and SERCR retain positive CRPSS of approximately 0.08–0.12. For ASO low-flow conditions, the longest available horizon is month 3; regional nCRPS is about 9–26% and CRPSS ranges from approximately −0.05 to 0.12, with SPP and TRE below climatology. Thus, long-lead hydropower value depends on both region and season and should not be inferred from an all-month mean alone.

Facility-level spatial patterns supporting these regional summaries are provided in Supporting Information Text S5 and Figures S6–S11.

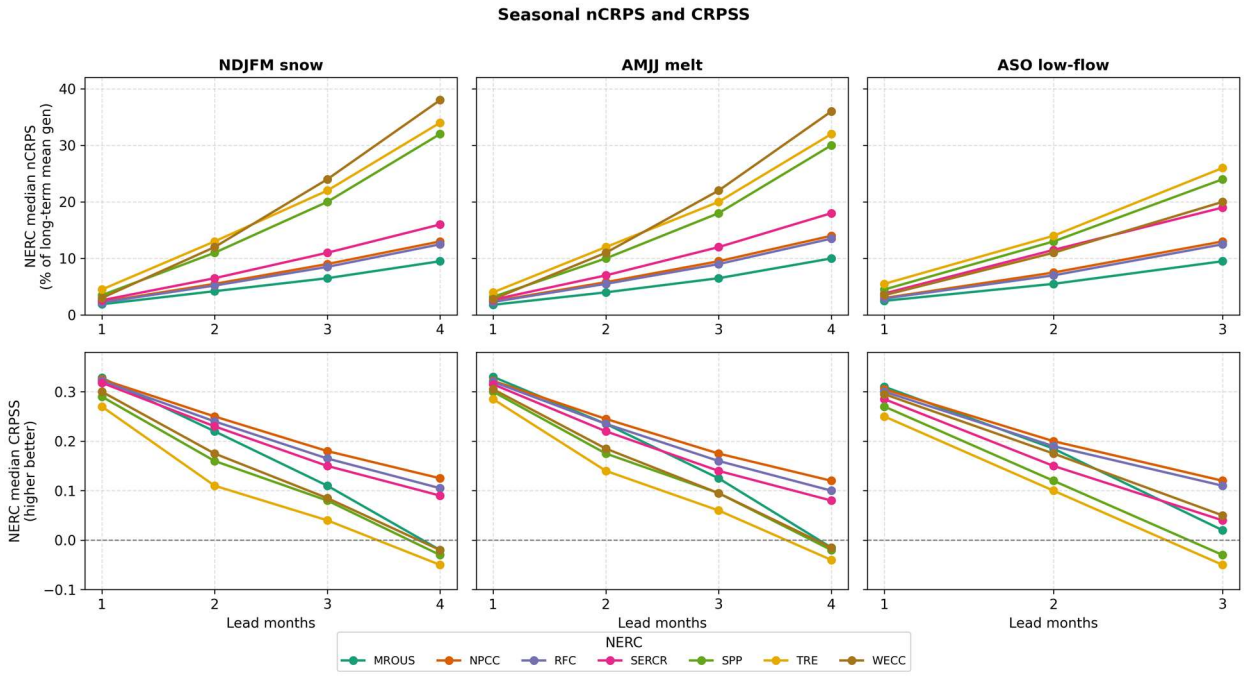


Figure 10. Seasonal NERC-region median hydropower nCRPS (top) and CRPSS relative to climatology (bottom) by lead for NDJFM snow season, AMJJ melt season, and ASO late-summer/early-fall low-flow season. *Lower nCRPS and higher CRPSS are better; the dashed line denotes zero CRPSS. ASO includes three lead months due to the seasonal window.*

5. Limitations

The evaluation identifies limitations at each stage of the prototype and constrains its intended use to regional probabilistic planning.

First, coarse NMME hindcasts and the MSWX training target introduce input uncertainty. FNO reduces MAE relative to the selected baselines but retains orographic precipitation, seasonal temperature, and wind biases. MSWX itself incorporates a fixed 1979–2013 CHELSA climatology; because MSWX is also the evaluation target, the present experiment cannot diagnose

bias relative to a current-climate station network. Periodic recalibration against updated observations is needed under non-stationary climate. The predominantly positive actual-forcing differences show that removing FNO improves KGE and CRPSS across much of the domain and that downscaling error is a substantial contributor to runoff error. However, localized non-positive differences and residual spatial heterogeneity show that bypassing FNO does not eliminate runoff error. The UMAL-LSTM lacks explicit snow accumulation and melt physics, and reference-data and spatial-scale limitations remain important in western basins.

Second, the water-management and hydropower components simplify operations. MOSART-WM applies generic and data-driven large-scale storage–release behavior and configured sectoral demand priorities, but the present setup is not dynamically re-optimized using seasonal forecasts and does not optimize plant-specific flood-control rule curves or distinguish turbine releases from spill. The downstream autoregression uses inflow, outflow, storage, and historical lags, but it does not compute storage–elevation–head relationships, forebay and tailwater levels, turbine efficiency, or forward release schedules. Electricity prices, outages, infrastructure changes, operator forecasts, time-varying multi-objective priorities, and non-stationary rule changes are omitted. Historical behavior may be captured implicitly, but it may not transfer to unusual floods, droughts, infrastructure changes, or altered policy.

Third, uncertainty accumulates across the chain. The USGS KGE of routed and managed streamflow is substantially more heterogeneous than the GRFR-based runoff evaluation, but it combines UMAL-LSTM runoff error with mosartwmpy/MOSART-WM routing and water-management error and therefore cannot isolate UMAL-LSTM performance. The controlled-forcing experiment identifies meteorological downscaling as a substantial contributor to runoff error but retains localized evidence of hydrologic-model, reference-data, and scale-related

595 limitations. The seasonal hydropower-generation CRPSS and nCRPS results show that full-year
596 averages mask important differences among snow, melt, and low-flow periods and provide the
597 appropriate basis for season-specific operational interpretation.

598 At extended leads, declining CRPSS and widening nCRPS limit direct market or plant-level
599 interpretation. Positive median skill in a region does not guarantee skill at every facility, and by
600 month four some regional-seasonal summaries approach or fall below climatology. Future work
601 should combine improved snow and soil-moisture representation with data assimilation, plant-
602 specific storage and head constraints, and decision models tied to operator or market objectives.

603 The framework also omits real-time assimilation of streamflow, snowpack, reservoir storage, river
604 levels, and unit outages, and its fitted relationships assume approximate stationarity over the
605 historical period. These omissions limit transfer to changing climate, infrastructure,
606 socioeconomic demand, and water-allocation priorities. They are future extensions rather than
607 capabilities of the current prototype.

608 # 6. Conclusions

609 We developed a modular prototype linking seasonal climate forecasts, FNO downscaling,
610 probabilistic UMAL-LSTM runoff, MOSART-WM routing and water management, and plant-
611 level autoregressive hydropower prediction. During 2011–2020, FNO reduced monthly spatially
612 averaged MAE relative to the best non-FNO baseline by 13.0% for precipitation, 16.3% for
613 temperature, and 6.2% for wind speed, although residual biases and complex-terrain errors
614 remained.

Runoff evaluation showed broad deterministic and probabilistic skill relative to the GRFR reanalysis target. Independent streamflow and controlled-forcing checks indicated substantial spatial heterogeneity and contributions from both meteorological downscaling and hydrologic-model limitations. Because the streamflow comparison reflects the integrated runoff, routing, and water-management chain, including management effects in modeled and observed flows, it should not be interpreted as a direct evaluation of UMAL-LSTM runoff.

Regional hydropower forecasts provided their clearest value at one month, with median CRPSS of approximately 0.25–0.33. Skill declined with lead and varied by region and season; by month four, several snow- and melt-season regional CRPSS values approached or fell below zero.

The framework is therefore best interpreted as a regional probabilistic planning prototype. It is not a replacement for plant-operator models because it does not explicitly represent plant-specific submonthly operations and constraints, including flood-control optimization, turbine release versus spill, dynamic hydraulic head, market dispatch, changing priorities, and non-stationary rule curves.

Within those limits, the workflow demonstrates a computationally efficient route from seasonal climate information to probabilistic hydropower indicators for resource-adequacy analysis. Priorities for further development are expanded independent observational validation, improved snow and state estimation, and closer coupling to plant- and region-specific decision constraints.

Acknowledgments

This research was supported by the North American Energy Reliability Model (NAERM). The computational work was performed using PNNL Institutional Computing at Pacific Northwest National Laboratory. PNNL is a multi-program national laboratory operated for the U.S.

Department of Energy (DOE) by Battelle Memorial Institute under Contract No. DE-AC05-76RL01830. Accordingly, the U.S. Government retains and the publisher, by accepting the article for publication, acknowledges that the U.S. Government retains a nonexclusive, paid-up, irrevocable, worldwide license to publish or reproduce the published form of this manuscript or allow others to do so, for U.S. Government purposes.

Conflict of Interest

The authors declare no conflicts of interest relevant to this study

Open Research

The NMME CanESM5 hindcasts are available through the IRI Data Library [Kirtman et al., 2014]. MSWX meteorological data are described by Beck et al. [2022], GRFR runoff by Yang et al. [2021], and HydroWIRES B1 hydropower data by Bracken et al. [2024]. USGS streamflow observations were obtained from USGS Water Data for the Nation [U.S. Geological Survey, 1994]. The code and derived hydropower estimates are archived at Zenodo [Konapala, 2026].

References

Aasgård, E.K., Fleten, SE., Kaut, M. et al., (2019). Hydropower bidding in a multi-market setting. Energy Syst 10, 543–565 https://doi.org/10.1007/s12667-018-0291-y

Beck, H. E., Van Dijk, A. I., Larraondo, P. R., McVicar, T. R., Pan, M., Dutra, E., & Miralles, D. G. (2022). MSWX: Global 3-hourly 0.1 bias-corrected meteorological data, including near-real-time updates and forecast ensembles. Bulletin of the American Meteorological Society, 103(3), E710-E732

Bracken, C., Rajagopalan, B., & Prairie, J. (2010). A multisite seasonal ensemble streamflow forecasting technique. *Water Resources Research*, *46*(3). https://doi.org/10.1029/2009WR007965

Bracken, C., Voisin, N., Broman, D., Turner, S. W. D., & Oikonomou, K. (2024). HydroWIRES B1: Monthly and Weekly Hydropower Constraints Based on Disaggregated EIA-923 Data (v1.3.0) [Data set]. Zenodo. https://doi.org/10.5281/zenodo.13351949

Bracken, C., Son, Y., Broman, D., & Voisin, N. (2025). GODEEEP-hydro: Historical and projected power system ready hydropower data for the United States. *Scientific Data*, *12*(1), 1-8. https://doi.org/10.1038/s41597-025-05097-3

Brando, A. S., Barros, P. H., & Duque, D. G. (2022). Uncountable Mixtures of Asymmetric Laplacians for High-Quality Uncertainty Quantification. arXiv preprint arXiv:2211.10132.

Broman, D., Voisin, N., Kao, S.-C., Fernandez, A. and Ghimire, G.R. 2024. Multi-scale impacts of climate change on hydropower for long-term water-energy planning in the contiguous United States. Environmental Research Letters 19(9), 094057. https://dx.doi.org/10.1088/1748-9326/ad6ceb

Cheng, M., Fang, F., Navon, I. M., & Pain, C. (2023). Ensemble Kalman filter for GAN-ConvLSTM based long lead-time forecasting. Journal of Computational Science, 69, 102024. https://doi.org/10.1016/j.jocs.2023.102024

Clark, M., Gangopadhyay, S., Hay, L., Rajagopalan, B., & Wilby, R. (2004). The Schaake shuffle: A method for reconstructing space–time variability in forecasted precipitation and temperature fields. Journal of Hydrometeorology, 5(1), 243-262.

677 Cosgrove, B., Gochis, D., Flowers, T., Dugger, A., Ogden, F., Graziano, T., Clark, E., Cabell, R.,
678 Casiday, N., Cui, Z., Eicher, K., Fall, G., Feng, X., Fitzgerald, K., Frazier, N., George, C., Gibbs,
679 R., Hernandez, L., Johnson, D., . . . Zhang, Y. (2024). NOAA's National Water Model: Advancing
680 operational hydrology through continental-scale modeling. JAWRA Journal of the American
681 Water Resources Association, 60(2), 247-272. https://doi.org/10.1111/1752-1688.13184

682 De Silva, T., Jorgenson, J., Macknick, J., Keohan, N., Miara, A., Jager, H., & Pracheil, B. (2022).
683 Hydropower operation in future power grid with various renewable power integration. Renewable
684 Energy Focus, 43, 329-339. https://doi.org/10.1016/j.ref.2022.11.001

685 Fang, Z., Qu, S., Li, Z., Li, Q., Shi, P., Sun, Y., Yang, X., Tang, H., Zhang, J., Zhu, Z., Wu, H., &
686 Bao, W. (2025). Soil Water Accounting Network (SWAN): A novel neural network for modeling
687 conceptual hydrological processes. Journal of Hydrology, 133562.
688 https://doi.org/10.1016/j.jhydrol.2025.133562

689 Frame, J.M., Araki, R., Bhuiyan, S.A., Bindas, T., Rapp, J., Bolotin, L., Deardorff, E., Liu, Q.,
690 Haces-Garcia, F., Liao, M., Frazier, N. and Ogden, F.L. (2025), Machine Learning for a
691 Heterogeneous Water Modeling Framework. J Am Water Resour Assoc, 61:
692 e70000. https://doi.org/10.1111/1752-1688.70000

693 Gaudard, L., Gabbi, J., Bauder, A., & Romerio, F. (2016). Long-term uncertainty of hydropower
694 revenue due to climate change and electricity prices. Water resources management, 30, 1325-
695 1343.

696 Gao, H., Birkett, C., & Lettenmaier, D. P. (2012). Global monitoring of large reservoir storage
697 from satellite remote sensing. Water Resources Research, 48, W09504.
698 https://doi.org/10.1029/2012WR012063

699 Gupta, H. V., Kling, H., Yilmaz, K. K., & Martinez, G. F. (2009). Decomposition of the mean
700 squared error and NSE performance criteria: Implications for improving hydrological modelling.
701 Journal of Hydrology, 377(1-2), 80-91. https://doi.org/10.1016/j.jhydrol.2009.08.003

702 Gutmann, E. D., Rasmussen, R. M., Liu, C., Ikeda, K., Gochis, D. J., Clark, M. P., ... & Thompson,
703 G. (2012). A comparison of statistical and dynamical downscaling of winter precipitation over
704 complex terrain. Journal of Climate, 25(1), 262-281.

705 Hansen, C. H., Ghimire, G. R., & Kao, S.-C. (2022). Evaluation of nominal energy storage at
706 existing hydropower reservoirs in the US. Water Resources Research, 58(11), e2022WR032210.
707 https://doi.org/10.1029/2022WR032210

708 Hamlet, A. F., Huppert, D., & Lettenmaier, D. P. (2002). Economic value of long-lead streamflow
709 forecasts for Columbia River hydropower. Journal of Water Resources Planning and
710 Management, 128(2), 91-101.

711 Hejazi, M.I., Voisin, N., Liu, L., Bramer, L.M., Fortin, D.C., Hathaway, J.E., Huang, M., Kyle, P.,
712 Leung, L.R., Li, H.-Y., Liu, Y., Patel, P.L., Pulsipher, T.C., Rice, J.S., Tesfa, T.K., Vernon, C.R.
713 and Zhou, Y. 2015. 21st century United States emissions mitigation could increase water stress
714 more than the climate change it is mitigating. Proceedings of the National Academy of Sciences
715 112(34), 10635.

716 Hester, E. T., Voisin, N., Griffiths, N. A., & Kao, C. (2025). Intersection of Hydrologic Change
717 and Hydropower in the United States: Needs for Future Research and Practice. *JAWRA Journal of*
718 *the American Water Resources Association*, *61*(3), e70020. https://doi.org/10.1111/1752-
719 1688.70020

720 Hersbach, H. (2000). Decomposition of the continuous ranked probability score for ensemble
721 prediction systems. Weather and Forecasting, 15(5), 559-570.

722 Hersbach, H., Bell, B., Berrisford, P., Hirahara, S., Horányi, A., Muñoz-Sabater, J., Nicolas, J.,
723 Peubey, C., Radu, R., Schepers, D., Simmons, A., Soci, C., Abdalla, S., Abellan, X., Balsamo, G.,
724 Bechtold, P., Biavati, G., Bidlot, J., Bonavita, M., . . . Thépaut, N. (2020). The ERA5 global
725 reanalysis. Quarterly Journal of the Royal Meteorological Society, 146(730), 1999-2049.
726 https://doi.org/10.1002/qj.3803

727 Jiang, P., Yang, Z., Wang, J., Huang, C., Xue, P., Chakraborty, T. C., Chen, X., & Qian, Y. (2023).
728 Efficient Super-Resolution of Near-Surface Climate Modeling Using the Fourier Neural Operator.
729 Journal of Advances in Modeling Earth Systems, 15(7), e2023MS003800.
730 https://doi.org/10.1029/2023MS003800

731 Johnson, J. M., Fang, S., Sankarasubramanian, A., Rad, A. M., Kindl da Cunha, L., Jennings, K.
732 S., et al. (2023). Comprehensive analysis of the NOAA National Water Model: A call for
733 heterogeneous formulations and diagnostic model selection. Journal of Geophysical Research:
734 Atmospheres, 128, e2023JD038534. https://doi.org/10.1029/2023JD038534

735 Karger, D. N., Conrad, O., Böhner, J., Kawohl, T., Kreft, H., Wilber, R., Zimmermann, N. E.,
736 Linder, H. P., & Kessler, M. (2017). Climatologies at high resolution for the earth's land surface
737 areas. Scientific Data, 4(1), 1-20. https://doi.org/10.1038/sdata.2017.122

738 Kirtman, B. P., Min, D., Infanti, J. M., Kinter III, J. L., Paolino, D. A., Zhang, Q., ... & Wood, E.
739 F. (2014). The North American multimodel ensemble: phase-1 seasonal-to-interannual prediction;
740 phase-2 toward developing intraseasonal prediction. Bulletin of the American Meteorological
741 Society, 95(4), 585-601.

742 Klotz, D., Kratzert, F., Gauch, M., Keefe Sampson, A., Brandstetter, J., Klambauer, G., ... &
743 Nearing, G. (2022). Uncertainty estimation with deep learning for rainfall–runoff
744 modeling. Hydrology and Earth System Sciences, 26(6), 1673-1693.

745 Knoben, W.J.M., Freer, J.E. and Woods, R.A. 2019. Technical note: Inherent benchmark or not?
746 Comparing Nash–Sutcliffe and Kling–Gupta efficiency scores. Hydrol. Earth Syst. Sci. 23(10),
747 4323-4331. https://hess.copernicus.org/articles/23/4323/2019/

748 Konapala, G., Kao, C., & Addor, N. (2020). Exploring Hydrologic Model Process Connectivity at
749 the Continental Scale Through an Information Theory Approach. Water Resources Research,
750 56(10), e2020WR027340. https://doi.org/10.1029/2020WR027340

751 Konapala, G. (2026). Code and dataset for "Seasonal hydropower forecast framework using a
752 combination of deep learning and physics-based methods" [Data set and software]. Zenodo.
753 https://doi.org/10.5281/zenodo.17401715
754 Kratzert, F., Klotz, D., Brenner, C., Schulz, K., & Herrnegger, M. (2018). Rainfall–runoff
755 modelling using Long Short-Term Memory (LSTM) networks. Hydrology and Earth System
756 Sciences, 22(11), 6005-6022

757 Kratzert, F., Klotz, D., Shalev, G., Nevo, S., & Nearing, G. S. (2019). Towards learning universal,
758 regional, and local hydrological behaviors via machine learning applied to large-sample datasets.
759 Hydrology and Earth System Sciences, 23(12), 5089-5110.

760 Leinonen, J., Guillaume, A., & Yuan, T. (2020). Stochastic super-resolution for downscaling
761 ensembles of meteorological simulations. IEEE Geoscience and Remote Sensing Letters, 18(9),
762 1540-1544.

763 Leung, L. R., Bader, D. C., Taylor, M. A., & McCoy, R. B. (2020). An introduction to the E3SM
764 special collection: Goals, science drivers, development, and analysis. Journal of Advances in
765 Modeling Earth Systems, 12, e2019MS001821. https://doi.org/10.1029/2019MS001821

766 Li, H., Wigmosta, M.S., Wu, H., Huang, M., Ke, Y., Coleman, A.M. and Leung, L.R. 2013. A
767 Physically Based Runoff Routing Model for Land Surface and Earth System Models. Journal of
768 Hydrometeorology 14(3), 808-828. https://journals.ametsoc.org/doi/abs/10.1175/JHM-D-12-
769 015.1

770 Li, Z., Kovachki, N., Azizzadenesheli, K., Liu, B., Bhattacharya, K., Stuart, A., & Anandkumar,
771 A. (2020). Fourier Neural Operator for Parametric Partial Differential Equations. ArXiv.
772 https://arxiv.org/abs/2010.08895

773 Li, Z., Zheng, H., Kovachki, N., Jin, D., Chen, H., Liu, B., ... & Anandkumar, A. (2024). Physics-
774 informed neural operator for learning partial differential equations. ACM/JMS Journal of Data
775 Science, 1(3), 1-27.

776 Lu, M., Lall, U., Robertson, A. W., & Cook, E. (2017). Optimizing multiple reliable forward
777 contracts for reservoir allocation using multitime scale streamflow forecasts. Water Resources
778 Research, 53(3), 2035-2050. https://doi.org/10.1002/2016WR019552

779 Maraun, D. (2013). Bias correction, quantile mapping, and downscaling: Revisiting the inflation
780 issue. Journal of Climate, 26(6), 2137-2143.

781 Mazrooei, A., T. Sinha, A. Sankarasubramanian, S. Kumar, and C. D. Peters-
782 Lidard (2015), Decomposition of sources of errors in seasonal streamflow forecasting over the
783 U.S. Sunbelt, *J. Geophys. Res. Atmos.*, 120, 11,809–11,825, doi:10.1002/2015JD023687

784 Pechlivanidis, I. G., Crochemore, L., Rosberg, J., & Bosshard, T. (2020). What Are the Key
785 Drivers Controlling the Quality of Seasonal Streamflow Forecasts? *Water Resources Research*,
786 *56*(6), e2019WR026987. https://doi.org/10.1029/2019WR026987

787 Rolnick, D., Donti, P. L., Kaack, L. H., Kochanski, K., Lacoste, A., Sankaran, K., ... & Bengio, Y.
788 (2022). Tackling climate change with machine learning. ACM Computing Surveys
789 (CSUR), 55(2), 1-96.

790 Schaefli, B. (2015). Projecting hydropower production under future climates: A guide for decision-
791 makers and modelers to interpret and design climate change impact assessments. Wiley
792 Interdisciplinary Reviews: Water, 2(4), 271-289. https://doi.org/10.1002/wat2.1083

793 Ssembatya H., J. Kern, N. Voisin, S. Steinschneider, and D.P. Broman. 2025. "The Relative
794 Influences of Hydrologic Information and Dams' Production Decisions on Electricity Price
795 Forecasts." Submitted to Applied Energy. PNNL-SA-209198.

796 Stephens, C., Lall, U., Johnson, F., & Marshall, L. (2021). Landscape changes and their hydrologic
797 effects: Interactions and feedbacks across scales. Earth-Science Reviews, 212, 103466.
798 https://doi.org/10.1016/j.earscirev.2020.103466

799 Sun, Y., Frew, B., Dalvi, S., & Dhulipala, S. C. (2022). Insights into methodologies and
800 operational details of resource adequacy assessment: A case study with application to a broader
801 flexibility framework. Applied Energy, 328, 120191.
802 https://doi.org/10.1016/j.apenergy.2022.120191

803 Thurber T.B., C.R. Vernon, N. Sun, S. Turner, J.J. Yoon, and N. Voisin (2021). mosartwmpy: A
804 Python implementation of the MOSART-WM coupled hydrologic routing and water management
805 model. Journal of Open-Source Software, 6(62), 3221. https://doi.org/10.21105/joss.03221

806 Troin, M., Arsenault, R., Wood, A. W., Brissette, F., & Martel, L. (2021). Generating Ensemble
807 Streamflow Forecasts: A Review of Methods and Approaches Over the Past 40 Years. Water
808 Resources Research, 57(7), e2020WR028392. https://doi.org/10.1029/2020WR028392

809 Turner, S. W., & Voisin, N. (2022). Simulation of hydropower at subcontinental to global scales:
810 a state-of-the-art review. Environmental Research Letters, 17(2), 023002.

811 Turner, S. W., Steyaert, J. C., Condon, L., & Voisin, N. (2021). Water storage and release policies
812 for all large reservoirs of conterminous United States. Journal of Hydrology, 603, 126843.
813 https://doi.org/10.1016/j.jhydrol.2021.126843

814 Turner, S. W., Voisin, N., & Nelson, K. (2022). Revised monthly energy generation estimates for
815 1,500 hydroelectric power plants in the United States. Scientific Data, 9(1), 1-11.
816 https://doi.org/10.1038/s41597-022-01748-x

817 Turner, S. W., Xu, W., & Voisin, N. (2020). Inferred inflow forecast horizons guiding reservoir
818 release decisions across the United States. Hydrology and Earth System Sciences, 24(3), 1275-
819 1291.

820 U.S. Geological Survey. (1994). USGS Water Data for the Nation [Data set].
821 https://doi.org/10.5066/F7P55KJN
822 Vandal, T., Kodra, E., Ganguly, S., Michaelis, A., Nemani, R., & Ganguly, A. R. (2017). DeepSD:
823 Generating high-resolution climate change projections through single image super-resolution.
824 Proceedings of the 23rd ACM SIGKDD international conference on knowledge discovery and data
825 mining, 1663-1672

826 Voisin, N., Li, H., Ward, D., Huang, M., Wigmosta, M., & Leung, L. R. (2013). On an improved
827 sub-regional water resources management representation for integration into earth system
828 models. Hydrology and Earth System Sciences, 17(9), 3605-3622. https://www.hydrol-earth-syst-
829 sci.net/17/3605/2013/

830 Voisin N, Pappenberger F, Lettenmaier DP, Buizza R, Schaake JC. Application of a Medium-
831 Range Global Hydrologic Probabilistic Forecast Scheme to the Ohio River Basin. Weather and
832 Forecasting. 2011;26(4):425–46. https://doi.org/10.1175/WAF-D-10-05032.1

833 Voisin, N., Hejazi, M. I., Leung, L. R., Liu, L., Huang, M., Li, Y., & Tesfa, T. (2017). Effects of
834 spatially distributed sectoral water management on the redistribution of water resources in an
835 integrated water model. Water Resources Research, 53(5), 4253-4270.
836 https://doi.org/10.1002/2016WR019767

837 Wilks, D.S. (2015), Multivariate ensemble Model Output Statistics using empirical copulas. Q.J.R.
838 Meteorol. Soc., 141: 945-952. https://doi.org/10.1002/qj.2414

839 Wood, A. W., T. Hopson, A. Newman, L. Brekke, J. Arnold, and M. Clark, 2016: Quantifying
840 Streamflow Forecast Skill Elasticity to Initial Condition and Climate Prediction Skill. *J.*
841 *Hydrometeor.*, **17**, 651–668, https://doi.org/10.1175/JHM-D-14-0213.1.

842 Yamazaki, D., Ikeshima, D., Sosa, J., Bates, P. D., Allen, G. H., & Pavelsky, T. M. (2019). MERIT
843 Hydro: A High-Resolution Global Hydrography Map Based on Latest Topography Dataset. Water
844 Resources Research, 55(6), 5053-5073. https://doi.org/10.1029/2019WR024873

845 Yang, Q., Harder, P., Ramesh, V., Sattegeri, P., Szwarcman, D., Watson, C. D., & Rolnick, D.
846 (2023). Fourier Neural Operators for Arbitrary Resolution Climate Data Downscaling. ArXiv.
847 https://arxiv.org/abs/2305.14452

848 Yang, Y., M. Pan, P. Lin, H. Beck, Z. Zeng, D. Yamazaki, C. David, H. Lu, K. Yang, Y. Hong,
849 and E. Wood, 2021: Global Reach-level 3-hourly River Flood Reanalysis (1980-2019).
850 BAMS, https://doi.org/10.1175/BAMS-D-20-0057.1

851 Yuan, X., Wood, E. F., & Ma, Z. (2015). A review on climate-model-based seasonal hydrologic
852 forecasting: Physical understanding and system development. Wiley Interdisciplinary Reviews:
853 Water, 2(5), 523-536. https://doi.org/10.1002/wat2.1088

854

Figure 01.

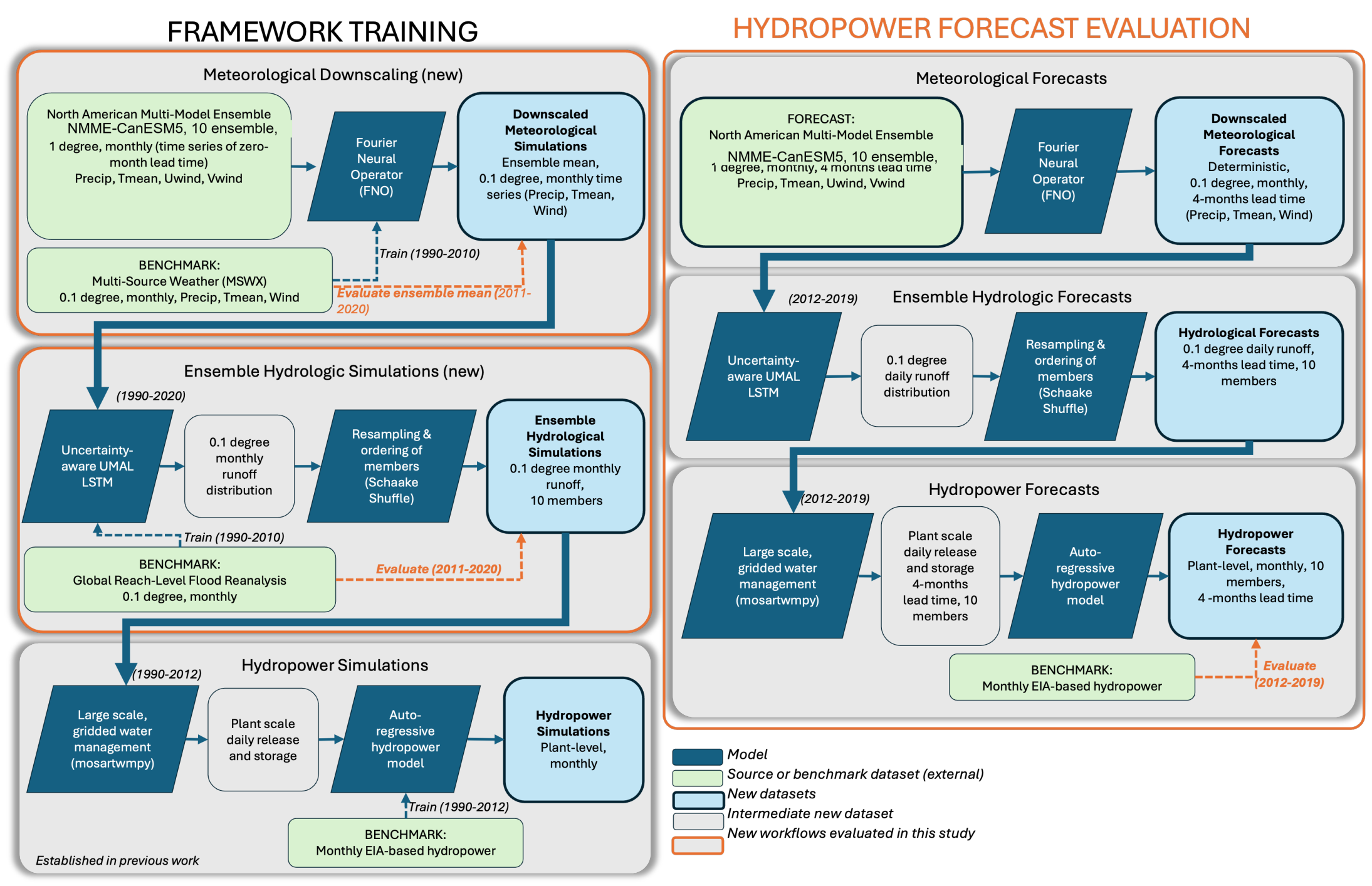

FRAMEWORK TRAINING
HYDROPOWER FORECAST EVALUATION
Meteorological Downscaling (new)
North American Multi-Model Ensemble
NMME-CanESM5, 10 ensemble,
1 degree, monthly (time series of zero-month lead time)
Precip, Tmean, Uwind, Vwind
Fourier Neural Operator (FNO)
Downscaled Meteorological Simulations
Ensemble mean,
0.1 degree, monthly time series (Precip, Tmean, Wind)
BENCHMARK:
Multi-Source Weather (MSWX)
0.1 degree, monthly, Precip, Tmean, Wind
Train (1990-2010)
Evaluate ensemble mean (2011-2020)
Ensemble Hydrologic Simulations (new)
(1990-2020)
Uncertainty-aware UMAL LSTM
0.1 degree monthly runoff distribution
Resampling & ordering of members (Schaake Shuffle)
Ensemble Hydrological Simulations
0.1 degree monthly runoff,
10 members
Train (1990-2010)
BENCHMARK:
Global Reach-Level Flood Reanalysis
0.1 degree, monthly
Evaluate (2011-2020)
Hydropower Simulations
(1990-2012)
Large scale, gridded water management (mosartwmpy)
Plant scale daily release and storage
Auto-regressive hydropower model
Hydropower Simulations
Plant-level, monthly
Train (1990-2012)
BENCHMARK:
Monthly EIA-based hydropower
Established in previous work
Meteorological Forecasts
FORECAST:
North American Multi-Model Ensemble
NMME-CanESM5, 10 ensemble,
1 degree, monthly, 4 months lead time
Precip, Tmean, Uwind, Vwind
Fourier Neural Operator (FNO)
Downscaled Meteorological Forecasts
Deterministic,
0.1 degree, monthly,
4-months lead time
(Precip, Tmean, Wind)
(2012-2019)
Ensemble Hydrologic Forecasts
Uncertainty-aware UMAL LSTM
0.1 degree daily runoff distribution
Resampling & ordering of members (Schaake Shuffle)
Hydrological Forecasts
0.1 degree daily runoff,
4-months lead time, 10 members
(2012-2019)
Hydropower Forecasts
Large scale, gridded water management (mosartwmpy)
Plant scale daily release and storage 4-months lead time, 10 members
Auto-regressive hydropower model
Hydropower Forecasts
Plant-level, monthly, 10 members,
4 -months lead time
BENCHMARK:
Monthly EIA-based hydropower
Evaluate (2012-2019)
Model
Source or benchmark dataset (external)
New datasets
Intermediate new dataset
New workflows evaluated in this study

Figure 02.

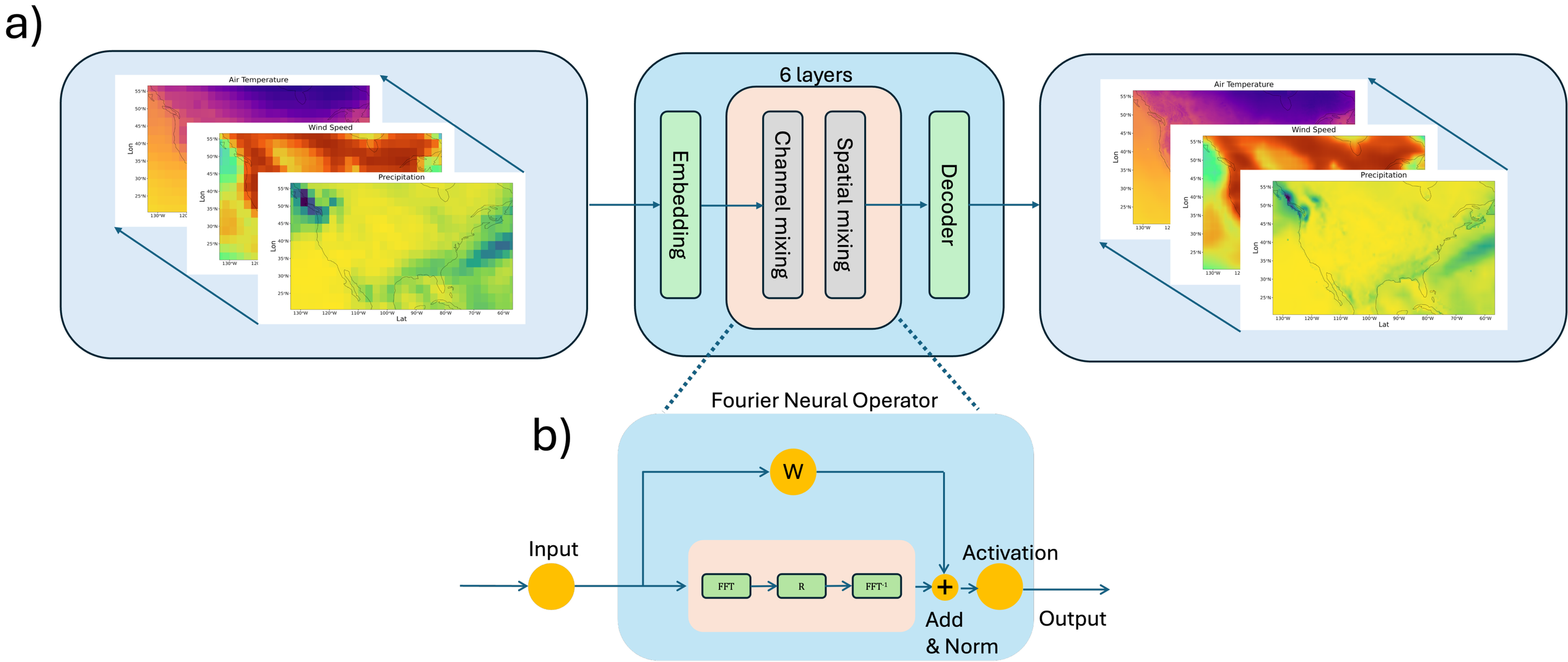

a)
Air Temperature
Wind Speed
Precipitation
Lon
Lat
6 layers
Embedding
Channel mixing
Spatial mixing
Decoder
Air Temperature
Wind Speed
Precipitation
Lon
Lat
b)
Fourier Neural Operator
W
Input
FFT
R
FFT-1
Activation
Add
& Norm
Output

Figure 03.

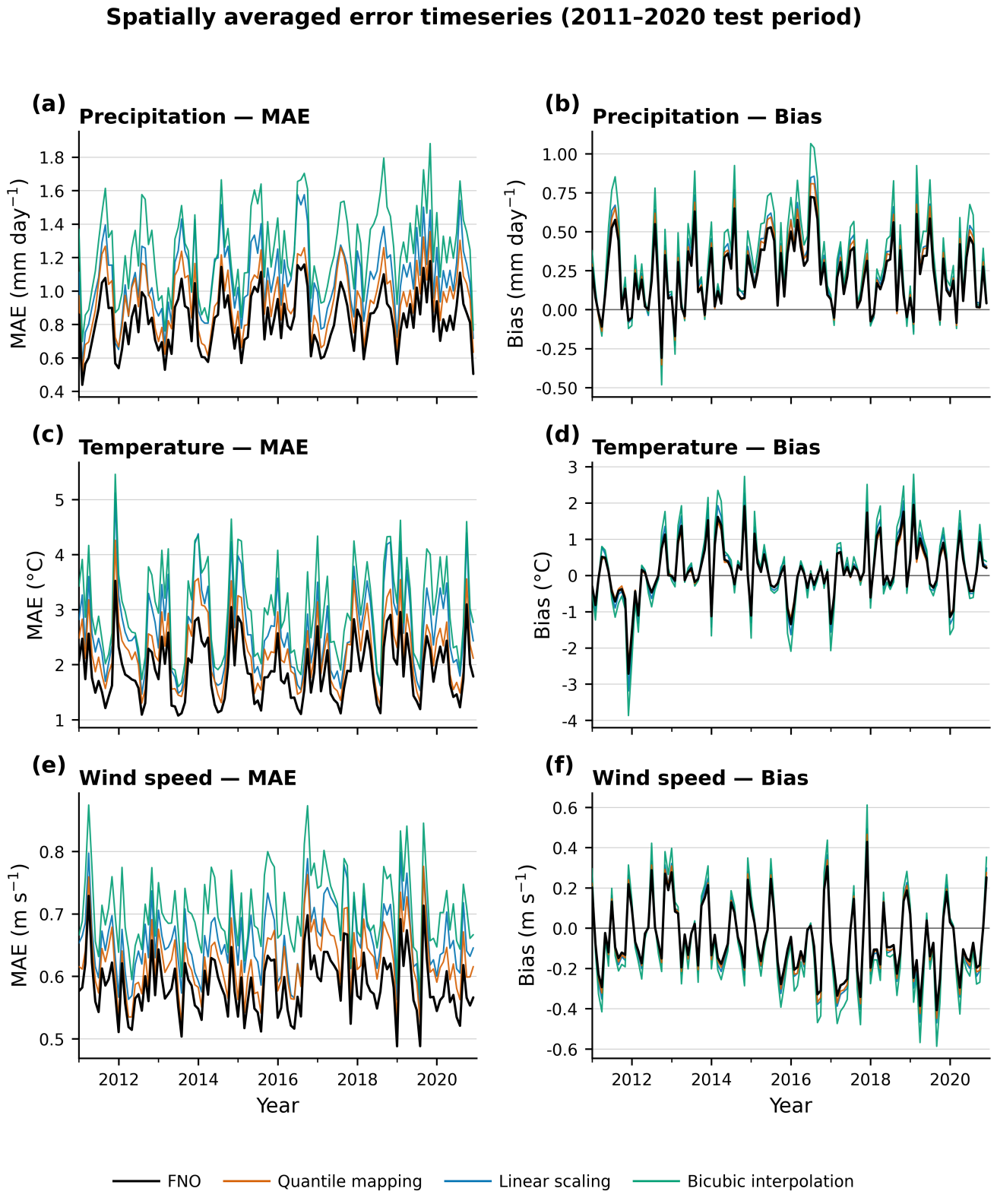
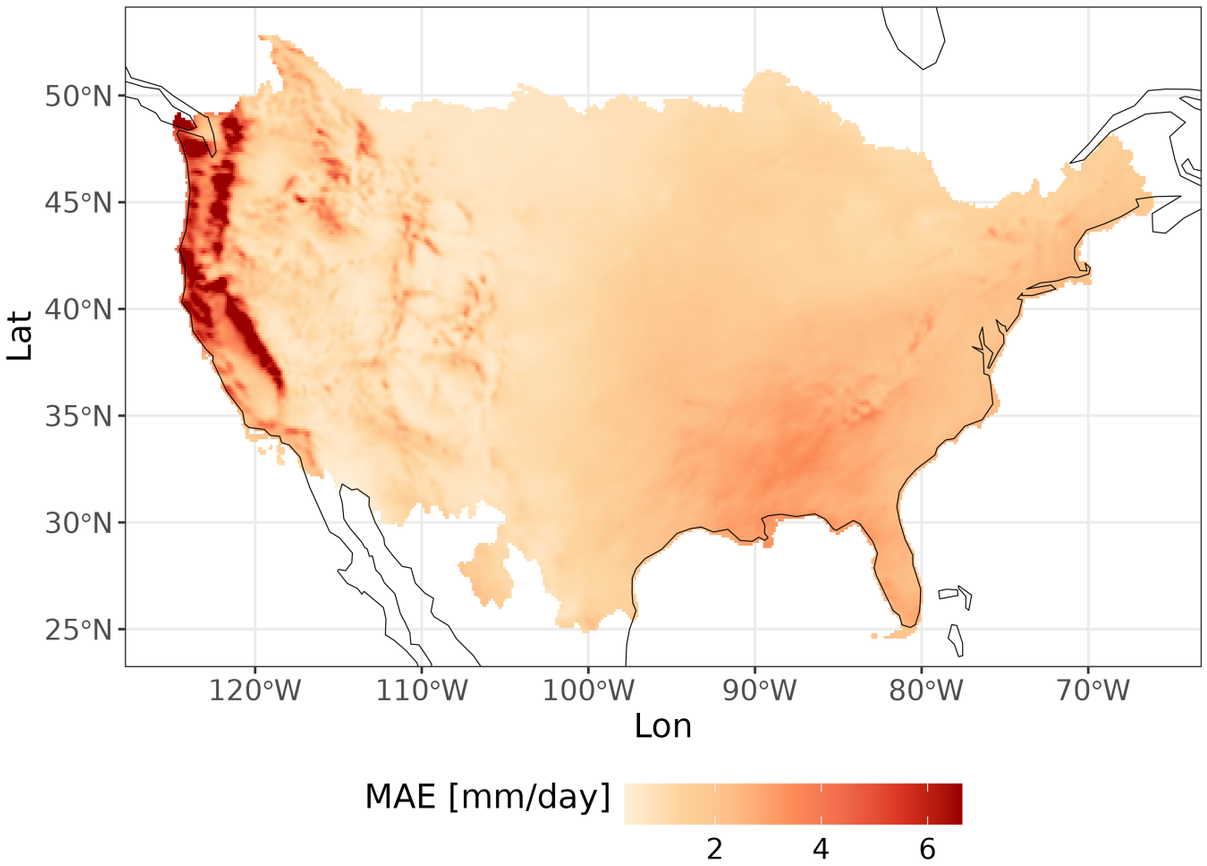

Spatially averaged error timeseries (2011–2020 test period)
(a)
Precipitation — MAE
MAE (mm day^{-1})
(b)
Precipitation — Bias
Bias (mm day^{-1})
(c)
Temperature — MAE
MAE (°C)
(d)
Temperature — Bias
Bias (°C)
(e)
Wind speed — MAE
MAE (m s^{-1})
(f)
Wind speed — Bias
Bias (m s^{-1})
2012
2014
2016
2018
2020
Year
FNO
Quantile mapping
Linear scaling
Bicubic interpolation

Figure 04.

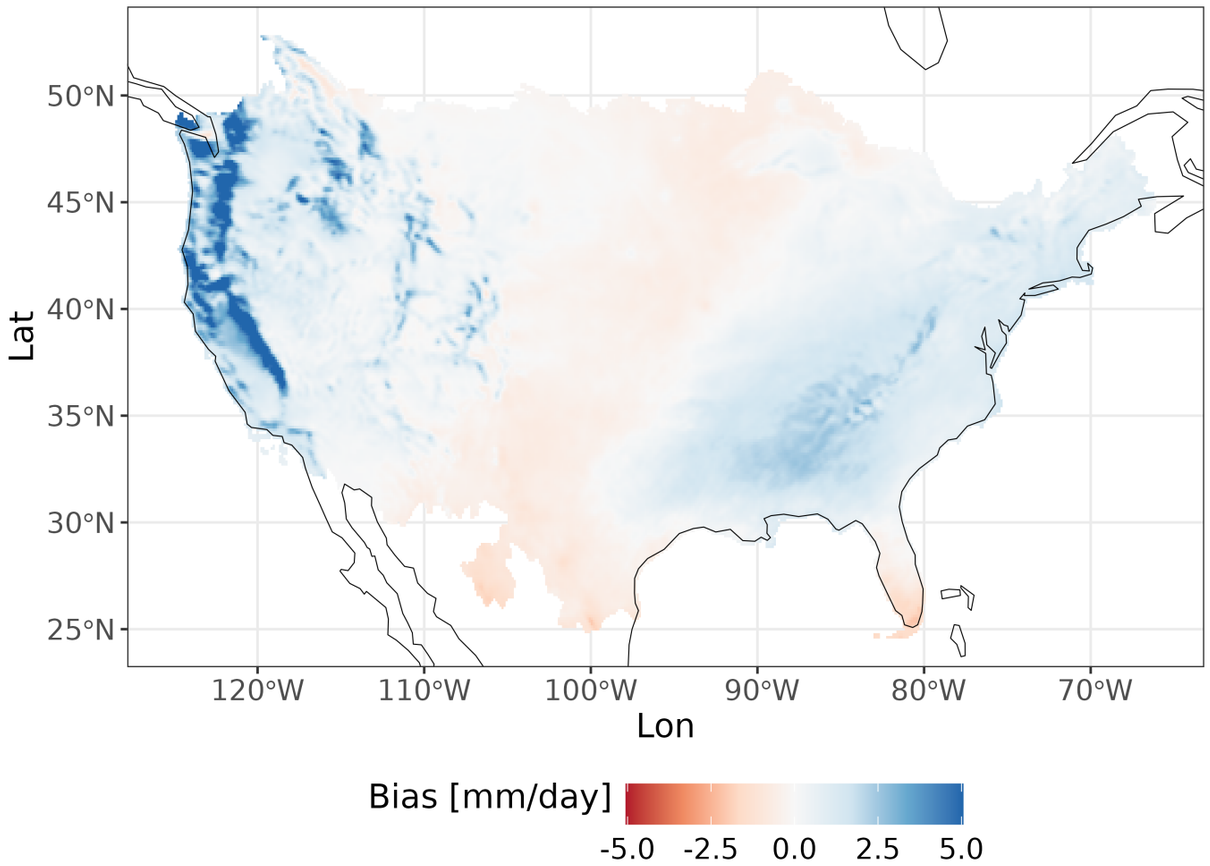
a

Precipitation [2011-2020] - MAE



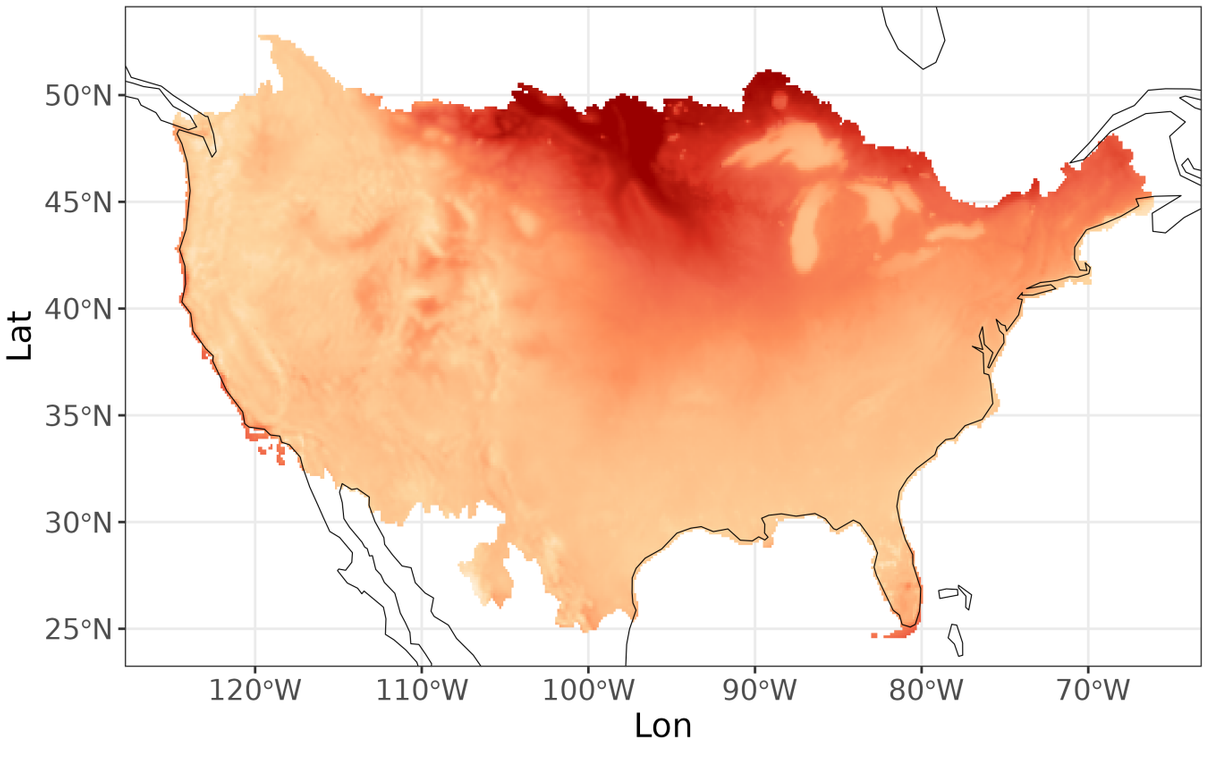
b

Precipitation [2011-2020] - Bias



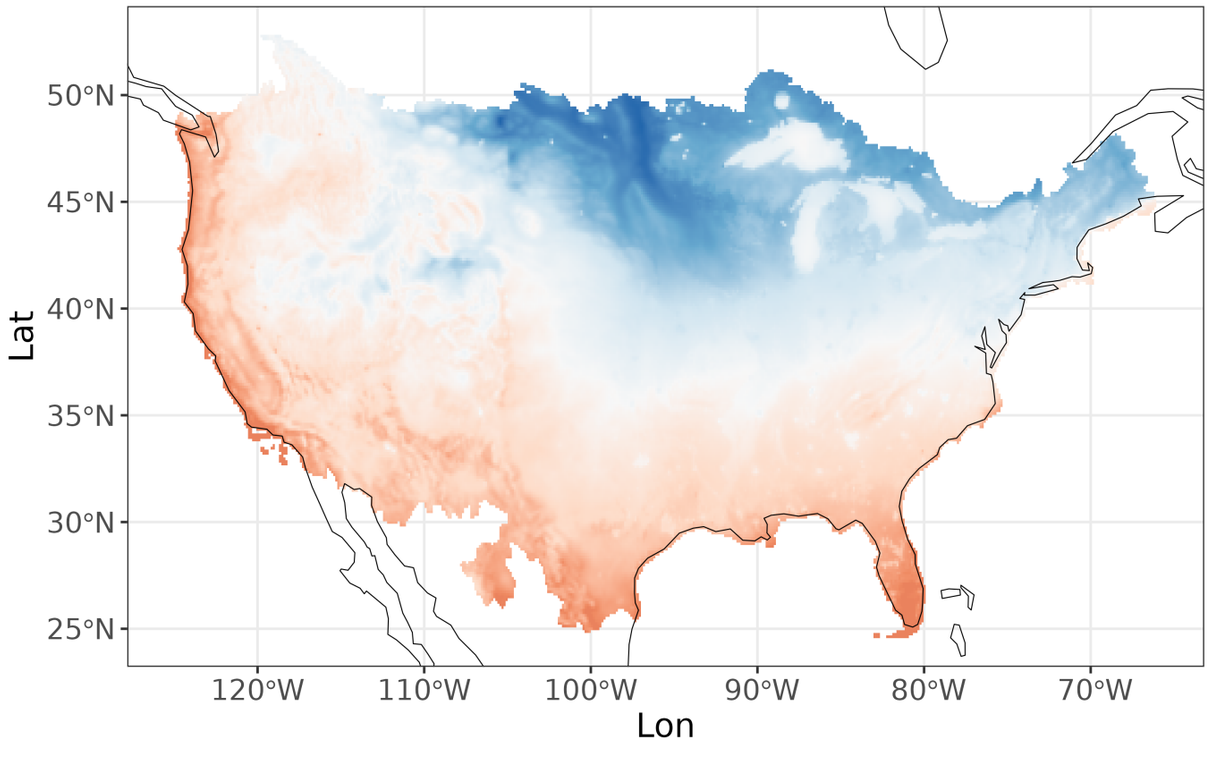
c

Temperature [2011-2020] - MAE



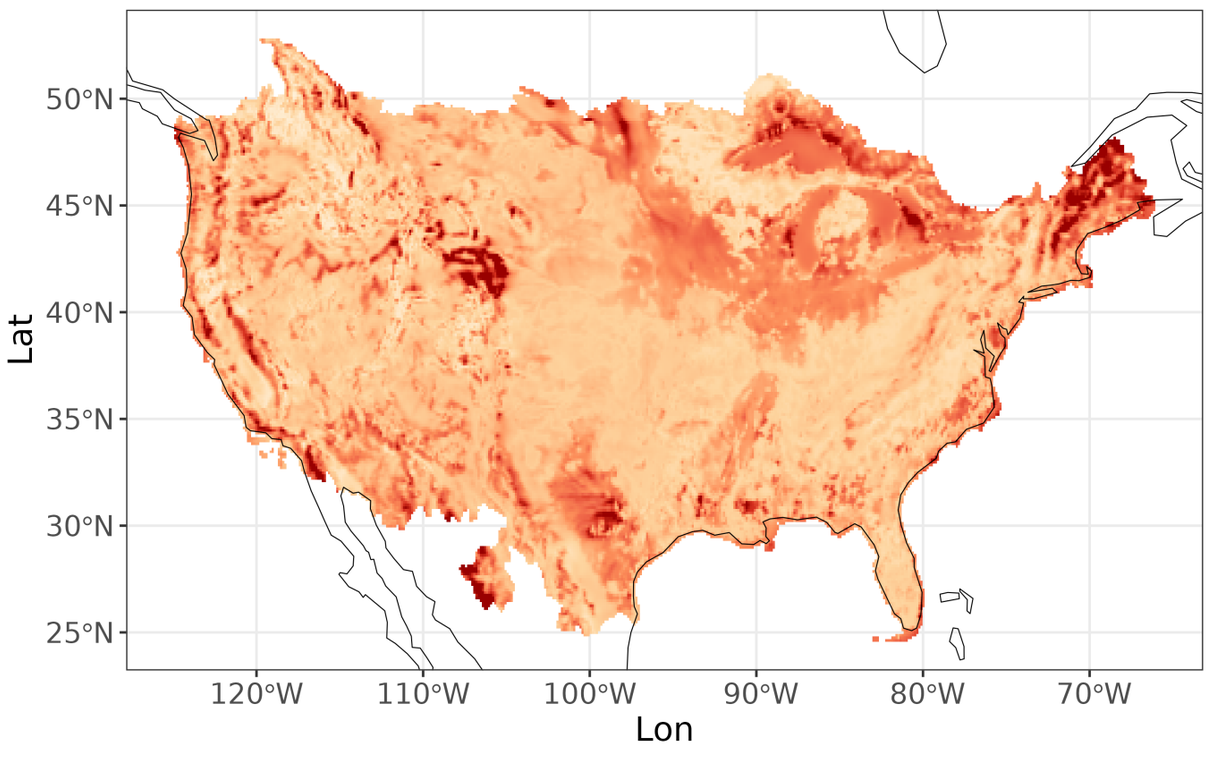
d

Temperature [2011-2020] - Bias



e

Wind Speed [2011-2020] - MAE



f

Wind Speed [2011-2020] - Bias

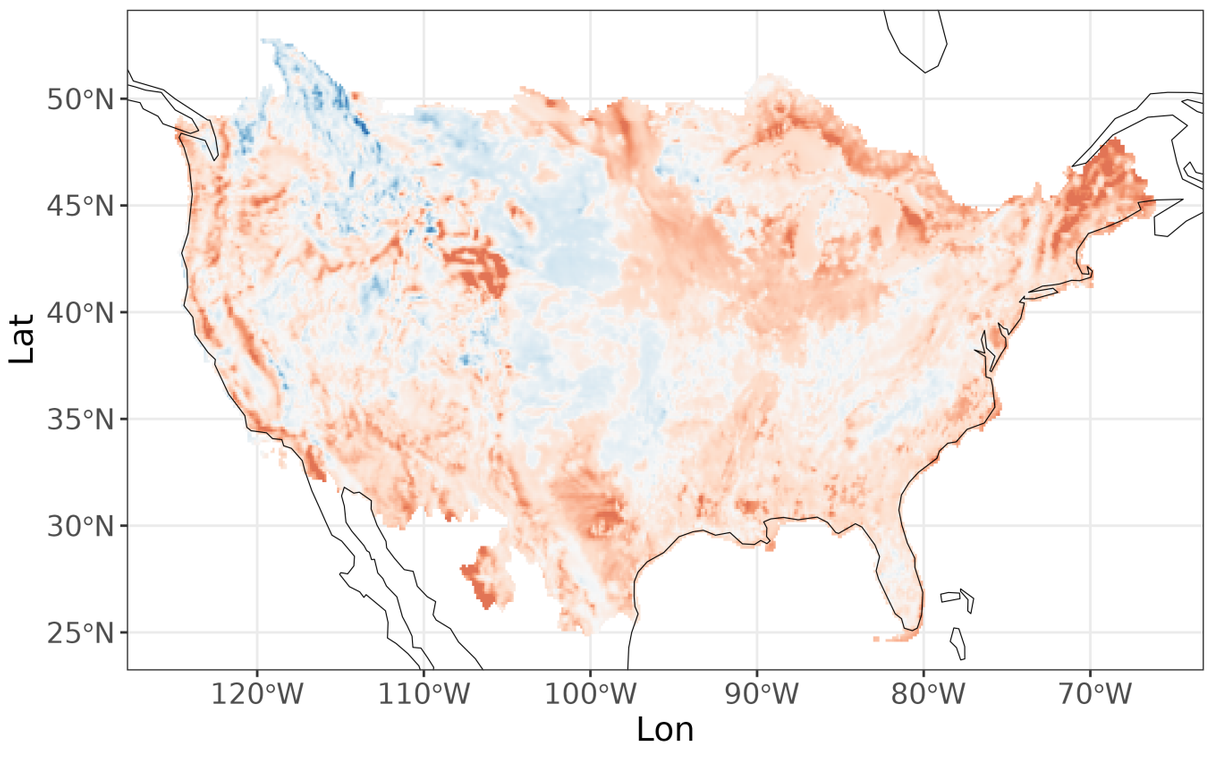


Figure 05.

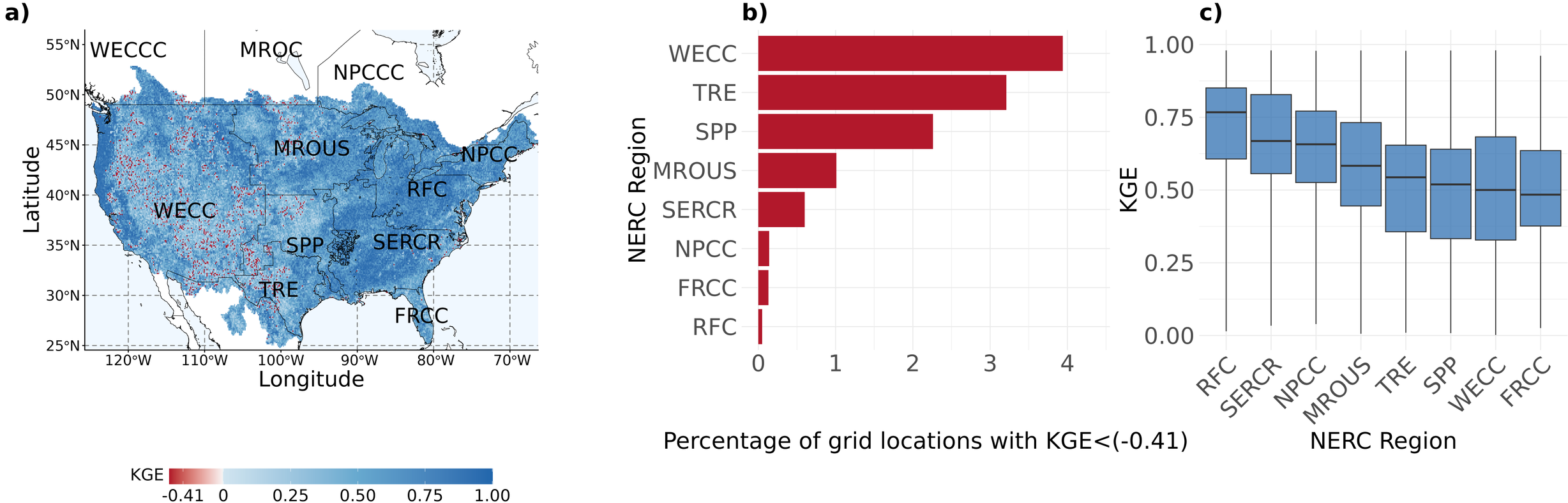

a)
WECCC
MROC
NPCCC
MROUS
NPCC
RFC
WECC
SPP
SERCR
TRE
FRCC
55°N
50°N
45°N
40°N
35°N
30°N
25°N
120°W
110°W
100°W
90°W
80°W
70°W
Latitude
Longitude
KGE
-0.41
0
0.25
0.50
0.75
1.00
b)
WECC
TRE
SPP
MROUS
SERCR
NPCC
FRCC
RFC
NERC Region
0
1
2
3
4
Percentage of grid locations with KGE<(-0.41)
c)
1.00
0.75
0.50
0.25
0.00
KGE
RFC
SERCR
NPCC
MROUS
TRE
SPP
WECC
FRCC
NERC Region

Figure 06.

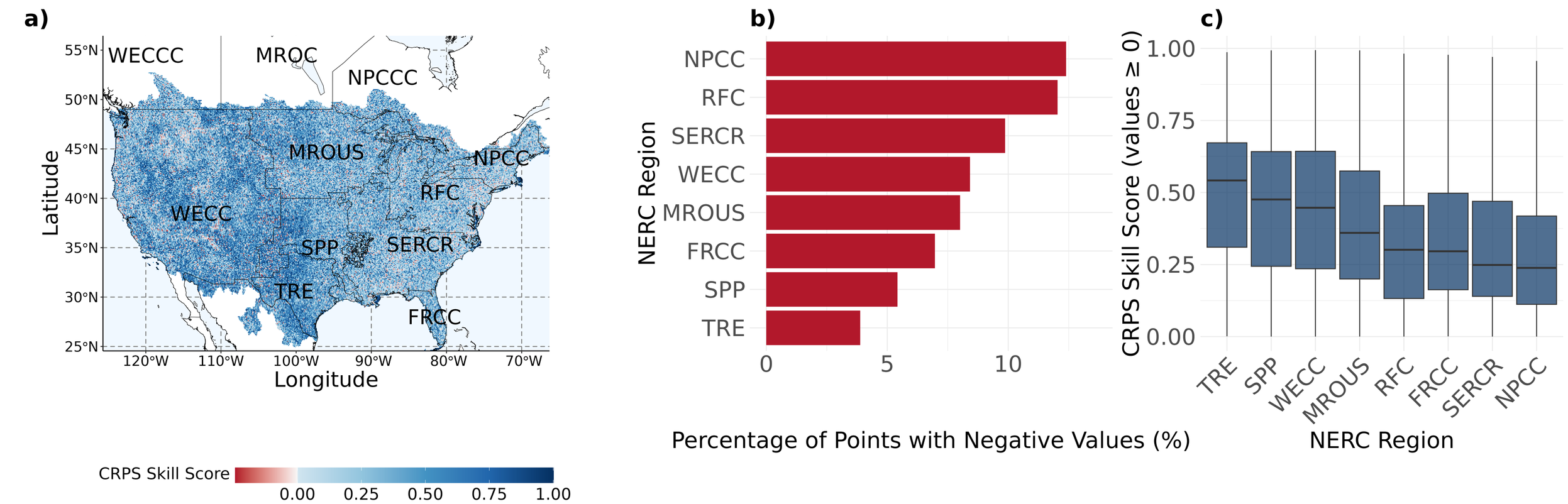

a)
WECCC
MROC
NPCCC
MROUS
NPCC
RFC
WECC
SPP
SERCR
TRE
FRCC
55°N
50°N
45°N
40°N
35°N
30°N
25°N
120°W
110°W
100°W
90°W
80°W
70°W
Latitude
Longitude
CRPS Skill Score
0.00
0.25
0.50
0.75
1.00
b)
NPCC
RFC
SERCR
WECC
MROUS
FRCC
SPP
TRE
NERC Region
0
5
10
Percentage of Points with Negative Values (%)
c)
CRPS Skill Score (values ≥ 0)
1.00
0.75
0.50
0.25
0.00
TRE
SPP
WECC
MROUS
RFC
FRCC
SERCR
NPCC
NERC Region

Figure 07.

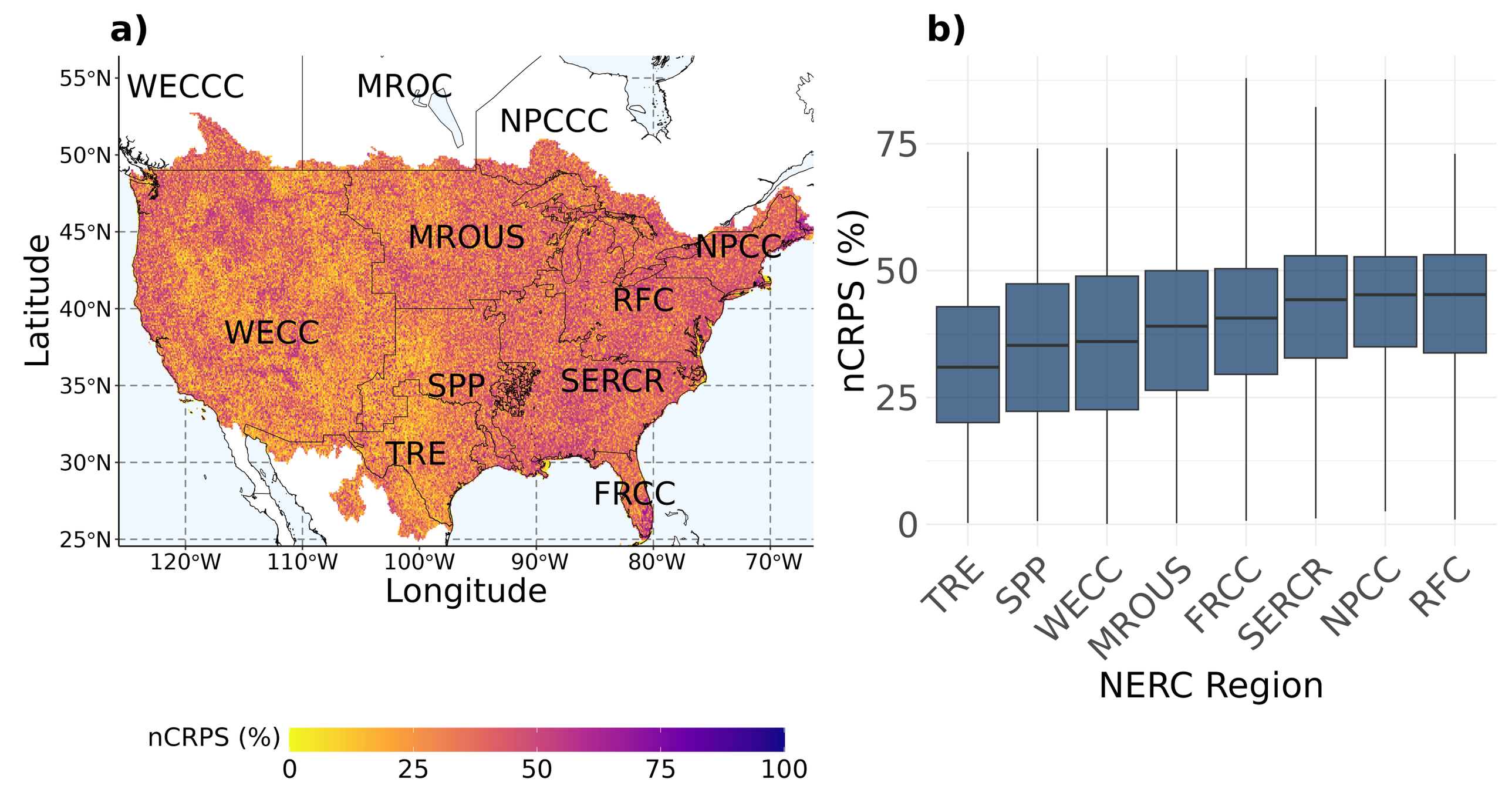

a)
WECCC
MROC
NPCCC
MROUS
NPCC
RFC
WECC
SPP
SERCR
TRE
FRCC
55°N
50°N
45°N
40°N
35°N
30°N
25°N
120°W
110°W
100°W
90°W
80°W
70°W
Latitude
Longitude
nCRPS (%)
0
25
50
75
100
b)
nCRPS (%)
0
25
50
75
TRE
SPP
WECC
MROUS
FRCC
SERCR
NPCC
RFC
NERC Region

Figure 08.

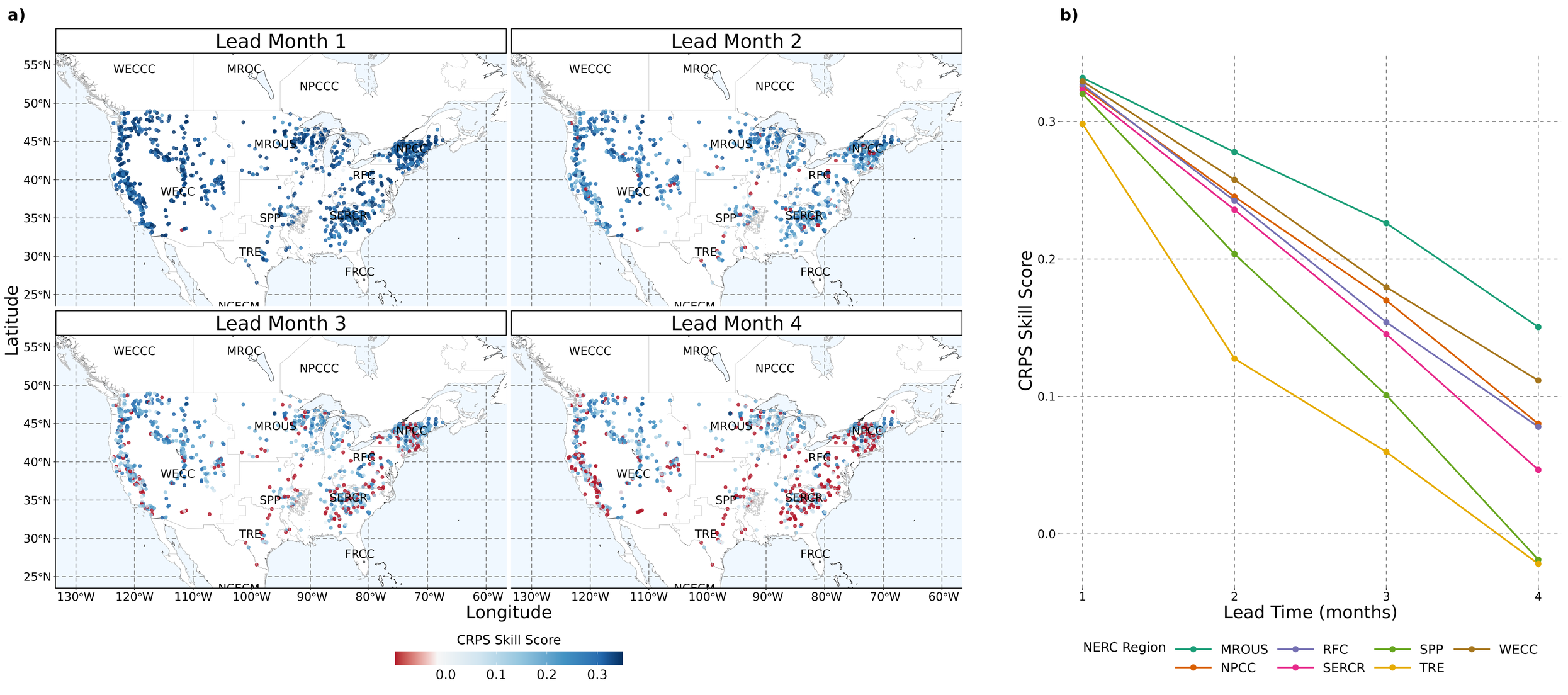

a)
Lead Month 1
Lead Month 2
Lead Month 3
Lead Month 4
WECCC
MROC
NPCCC
MROUS
NPCC
RFC
WECC
SPP
SERCR
TRE
FRCC
NCEC
55°N
50°N
45°N
40°N
35°N
30°N
25°N
130°W
120°W
110°W
100°W
90°W
80°W
70°W
60°W
Latitude
Longitude
CRPS Skill Score
0.0
0.1
0.2
0.3
b)
CRPS Skill Score
Lead Time (months)
1
2
3
4
NERC Region
MROUS
NPCC
RFC
SERCR
SPP
TRE
WECC

Figure 09.

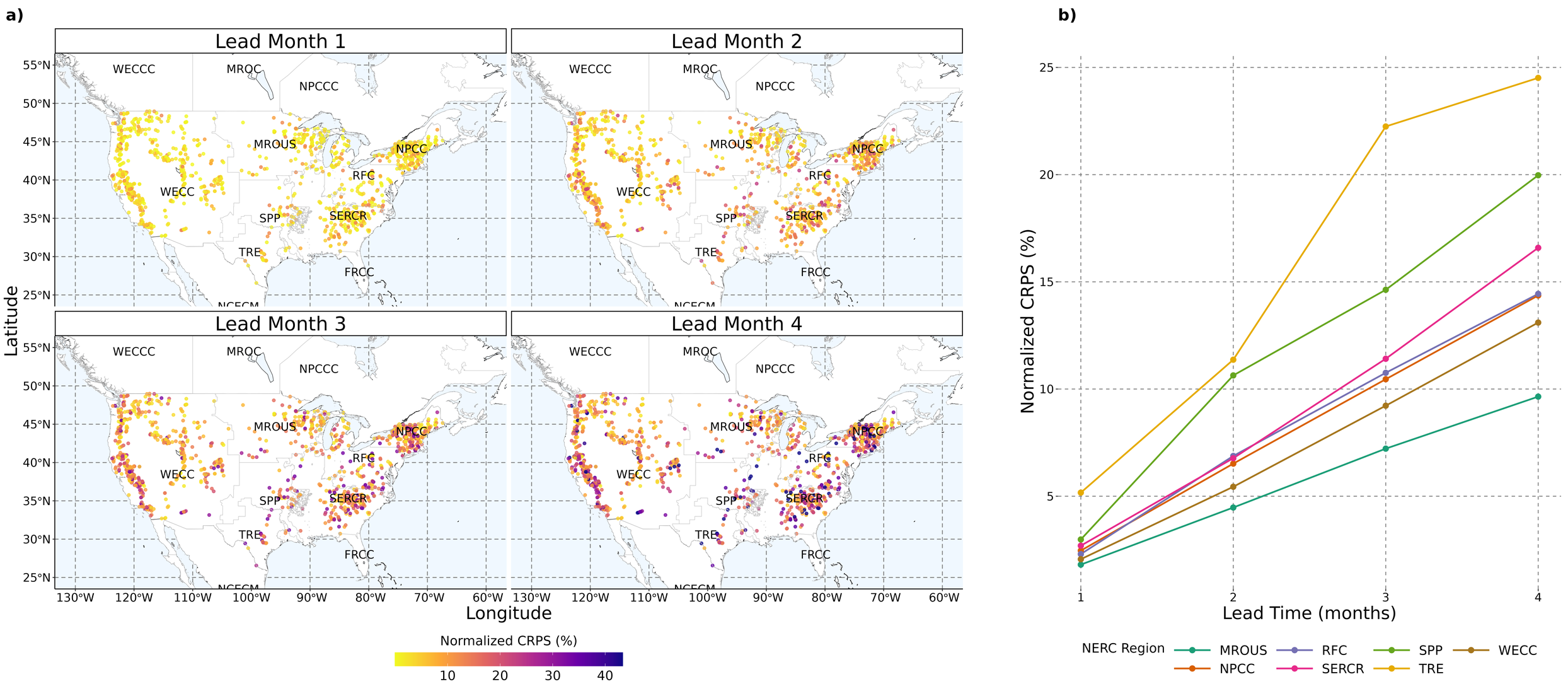
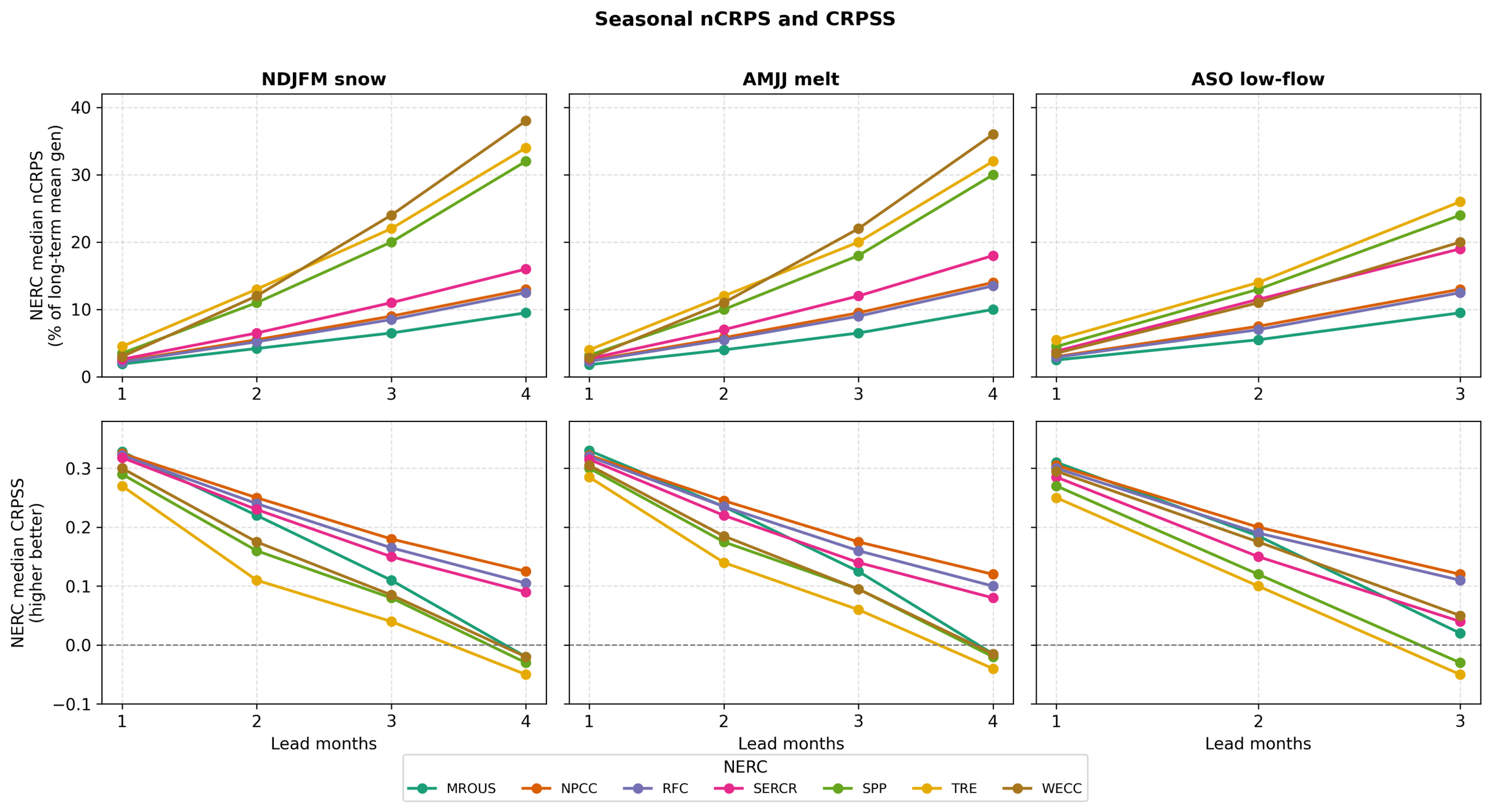

a)
Lead Month 1
Lead Month 2
Lead Month 3
Lead Month 4
WECCC
MRQC
NPCCC
MROUS
NPCC
RFC
WECC
SPP
SERCR
TRE
FRCC
NCFCM
55°N
50°N
45°N
40°N
35°N
30°N
25°N
130°W
120°W
110°W
100°W
90°W
80°W
70°W
60°W
Latitude
Longitude
Normalized CRPS (%)
10
20
30
40
b)
Normalized CRPS (%)
Lead Time (months)
NERC Region
MROUS
RFC
SPP
WECC
NPCC
SERCR
TRE

Figure 10.


Seasonal nCRPS and CRPSS
NDJFM snow
AMJJ melt
ASO low-flow
NERC median nCRPS
(% of long-term mean gen)
NERC median CRPSS
(higher better)
Lead months
Lead months
Lead months
NERC
MROUS
NPCC
RFC
SERCR
SPP
TRE
WECC